1-1-2012

Analysis Of A Parallel Stratiform Mesoscale Convective System During The Midlatitude Continental Convective Clouds Experiment

Andrea Neumann

ANALYSIS OF A PARALLEL STRATIFORM MESOSCALE CONVECTIVE SYSTEM DURING THE MIDLATITUDE CONTINENTAL CONVECTIVE CLOUDS EXPERIMENT

by

Andrea J. Neumann
Bachelor of Science, University of North Dakota, 2009

A Thesis

Submitted to the Graduate Faculty

Of the
University of North Dakota

In partial fulfillment of the requirements

for the degree of

Master of Science

Grand Forks, North Dakota
August
2012

This thesis, submitted by Andrea J. Neumann in partial fulfillment of the requirements for the Degree of Master of Arts from the University of North Dakota, has been read by the Faculty Advisory Committee under whom the work has been done, and is hereby approved.

_____
Michael Poellot

_____
David Delene

_____
Mark Askelson

This thesis is being submitted by the appointed advisory committee as having met all of the requirements of the Graduate School at the University of North Dakota and his hereby approved.

_____
Wayne Swisher
Interim Dean of the Graduate School

_____
Date

Title Analysis of a Parallel Stratiform Mesoscale Convective System during the Midlatitude Continental Convective Clouds Experiment

Department Atmospheric Sciences

Degree Master of Science

In presenting this thesis in partial fulfillment of the requirements for a graduate degree from the University of North Dakota, I agree that the library of this University shall make it freely available for inspection. I further agree that permission for extensive copying for scholarly purposes may by granted by the professor who supervised my thesis work or, in his absence, by the Chairperson of the department or the dean of the Graduate School. It is understood that any copying or publication or other use of this thesis or part thereof for financial gain shall not be allowed without my written permission. It is also understood that due recognition shall be given to me and to the University of North Dakota in any scholarly use which may be made of any material in my thesis.

Signature Andrea Neumann

Date July 26, 2012

TABLE OF CONTENTS

TABLE OF CONTENTS iv

LIST OF FIGURES vi

LIST OF TABLES xii

ACKNOWLEDGEMENTS xiii

ABSTRACT xiv

CHAPTER

I. INTRODUCTION AND BACKGROUND 1

Classification of Mesoscale Convective Systems 1

Impacts of PS MCS 5

Past Research on Trailing Stratiform (TS) and Leading Stratiform (LS) Mesoscale Convective Systems (MCSs) 6

Past Research on Parallel-Stratiform Type Mesoscale Convective Systems 9

Overview of the Midlatitude Continental Convective Clouds Experiment (MC3E) 10

II. DATA 12

Synoptic Analysis Data 12

Mesoscale Analysis Data 12

Sounding Data 13

Doppler Radar Data 15

Citation Microphysical Data 17

III. METHODOLOGY 22

Sounding Analysis 22

Doppler Radar Velocity Analysis 23

Citation Microphysical Data Analysis 24

IV. RESULTS AND DISCUSSION 30

Synoptic, Mesoscale, and Thermodynamic Environment 30

Wind Flow In and Around the MCS 46

Parallel Stratiform Region Microphysics 59

V. SUMMARY AND CONCLUSIONS 75

REFERENCES 79

LIST OF FIGURES

Figure Page

1. Conceptual model of a mesoscale convective system (MCS) with trailing stratiform (TS) region viewed in a vertical cross section oriented perpendicular to the convective line and parallel to its motion. Arrows represent storm-relative wind through the MCS. Reproduced from Houze et al. (1989). 2

2. Conceptual model of a mesoscale convective system (MCS) with leading stratiform (LS) region based on compiled radar observations of a front-fed convective line. This vertical cross section is oriented perpendicular to the convective line and parallel to its motion. Reproduced from Parker and Johnson (2004). 4

3. Conceptual model of a mesoscale convective system (MCS) with a parallel stratiform (PS) region based on compiled radar observations of a convective line. In this schematic three-dimensional rendering, the orientation of the vertical planes is perpendicular to the convective line and parallel to its motion. Reproduced from Parker (2007). 5

4. Map of National Weather Service (NWS) sounding launch sites (green push pins), Department of Energy (DOE) Atmospheric Radiation Measurement (ARM) sounding launch sites (yellow push pins), NWS Weather Surveillance Radars 88-Doppler (WSR-88D) locations (green balloons), and NASA S-Band Transportable Dual Polarimetric Radar (NPOL) location (blue balloon). The multi-colored line depicts the Citation flight track on 11 May 2011. 14

5. Sample ten-second spectrum from 17:17:29 UTC on 11 May 2011 showing a fitted gamma function that has a positive μ and a positive λ. The solid line is the function $N(D)=2.41*10^{-4}*D^{0.00727}*\exp(-39.7*D)$. 27

6. Sample ten-second spectrum from 17:16:49 UTC on 11 May 2011 showing a fitted gamma function that has a negative μ and positive λ. Solid line is the function $N(D)=2.72*10^{-7}*D^{-1.05}*\exp(-20.9*D)$. 27

7. Sample ten-second spectrum from 16:52:09 UTC on 11 May 2011 showing a bimodal spectrum with two fitted gamma functions. The first fitted function has a positive μ and a positive λ and the second fitted function has a negative μ and a negative λ. The combined function fit is represented by: $N(D)=5.23*10^{-3}*D^{0.282}*\exp(-385*D)$ when D <= 120 µm (dashed line) and $N(D)=5.72*10^{-13}*D^{-3.92}*\exp(12.5*D)$ when D > 120 µm (solid line). 28

8. Sample ten-second spectrum from 16:51:39 UTC showing a bimodal spectrum with the second gamma function having a λ greater than 100 cm^{-1}. The combined function fit is represented by: $N(D)=4.09*10^{-9}*D^{-2.01}*\exp(-27.2*D)$ when D <= 225 µm (dashed line) and $N(D)=6.47*10^{-6}*D^{-1.13}*\exp(234*D)$ when D > 225 µm (solid line). 29

9. 250 hPa geopotential height in meters (black contours) and isotachs in knots (colored contours) at 12 UTC on 11 May 2011 over the continuous United States. The star denotes location of ARM Central Facility in this and subsequent figures. Image courtesy of the Plymouth State Weather Center. 31

10. Surface observations, objectively analyzed surface pressure contours (blue), objectively analyzed frontal positions, national base radar reflectively mosaic, Storm Prediction Center (SPC) Severe Thunderstorm watch boxes (yellow boxes) for 12 UTC 11 May 2012. Image courtesy of Unisys Weather Image and Map Archive. 32

11. 500 hPa observations, 500 hPa geopotential height (black contours), and 500 hPa temperature (dashed red contours) at 12 UTC on 11 May 2012. Image courtesy of the Storm Prediction Center. 33

12. 700 hPa upper air observations, geopotential height (solid black contours), temperature (dashed red contours), and dew point when the dew point is greater than -4 °C (green contours) for 12 UTC 11 May 2011. Image courtesy of the Storm Prediction Center. 34

13. 850 hPa upper air observations, geopotential height (solid black contours), temperature (dashed red contours), and dew point when the dew point is greater than 8 °C (green contours) for 12 UTC 11 May 2012. Image courtesy of the Storm Prediction Center. 34

14. Base radar reflectivity over the central plains for the following times on 11 May 2012: (a) 11:55 UTC, (b) 12:54 UTC, (c) 13:53 UTC, (d) 14:52 UTC,

(e) 15:47 UTC, (f) 16:50 UTC, (g) 17:56 UTC, (h) 18:45 UTC, (i) 19:51 UTC, (j) 20:54 UTC, (k) 21:54 UTC, (l) 22:52 UTC. 36

15. Storm Prediction Center's (SPC) 300 hPa mesoanalysis product with 300 hPa geopotential height in black contours, 300 hPa divergence in magenta contours, and 300 hPa wind for the following times: (a) 12 UTC 11 May, (b) 15 UTC 11 May, (c) 18 UTC 11 May, and (d) 21 UTC 11 May. 39

16. Storm Prediction Center's (SPC) surface-based Convective Available Potential Energy (CAPE) mesoanalysis product showing surface-based CAPE in red contours and surface-based Convective Inhibition (CINH) in filled contours, and surface wind by wind barbs for the following times on 11 May 2011: (a) 12 UTC, (b) 15 UTC, (c) 18 UTC, and (d) 21 UTC. 40

17. Atmospheric sounding from the ARM Central Facility at 12 UTC on 11 May 2011. 41

18. Atmospheric sounding launched from the ARM Central Facility at 17 UTC 11 May 2011. 43

19. Atmospheric Soundings from Midlatitude Continental Convective Cloud Experiment (MC3E) outer launch site in Purcell, Oklahoma at 00 UTC 12 May 2011. 44

20. Contoured surface temperature (red) and surface-based cloud cover observations (circles) for each hour from 15 to 20 UTC, inclusive. The 70 °F isotherms are highlighted in thick red line. Images courtesy of Plymouth State Weather Center. 45

21. Wind direction (black) and wind speed (red) from the UND Citation on 11 May 2011. There are six level flight legs: (a) east to west flight leg at 7.5 km MSL, (b) west to east flight leg at 6.6 km MSL, (c) east to west flight leg at 5.6 km MSL, (d) west to east flight leg at 4.7 km MSL, (e) east to west flight leg at 3.7 km MSL, and (e) west to east flight leg at 2.8 km MSL..... 47

22. Radial velocity CAPPIs at 7.4 km MSL from (a) Vance Air Force Base, Oklahoma (KVNX) radar on 11 May 2011 at 16:55 UTC and (b) Wichita, Kansas (KICT) radar at 16:56 UTC. Arrow indicates wind direction across the zero isodop. 49

23. Radial velocity CAPPIs at 5.6 km MSL from (a) Vance Air Force Base, Oklahoma (KVNX) radar on 11 May 2011 at 16:55 UTC and (b) Wichita,

Kansas (KICT) radar at 16:56 UTC. Arrow indicates wind direction across the zero isodop. 50

24. Radial velocity CAPPIs at 3.7 km MSL from (a) Vance Air Force Base, Oklahoma (KVNX) radar on 11 May 2011 at 16:55 UTC and (b) Wichita, Kansas (KICT) radar at 16:56 UTC. Arrow indicates wind direction across the zero isodop. 51

25. Radial velocity CAPPIs at 7.4 km MSL from (a) Vance Air Force Base, Oklahoma (KVNX) radar on 11 May 2011 at 18:09 UTC and (b) Wichita, Kansas (KICT) radar at 18:10 UTC. Arrows indicate wind direction across the zero isodop. 52

26. Radial velocity CAPPIs at 5.6 km MSL from (a) Vance Air Force Base, Oklahoma (KVNX) radar on 11 May 2011 at 18:09 UTC and (b) Wichita, Kansas (KICT) radar at 18:10 UTC. Arrows indicate wind direction across the zero isodop. 53

27. Radial velocity CAPPIs at 3.7 km MSL from (a) Vance Air Force Base, Oklahoma (KVNX) radar on 11 May 2011 at 18:09 UTC and (b) Wichita, Kansas (KICT) radar at 18:10 UTC. Arrow indicates wind direction across the zero isodop. 54

28. NASA S-Band Transportable Dual Polarimetric Radar (NPOL) Relative Height Indicator (RHI) scans showing ground-relative radial velocity (in color, m s^{-1}) and storm-relative radial velocity (arrows, m s^{-1}) along the 270° radial (due west) for the following times on 11 May 2011: (a) 16:55, (b) 18:08 UTC. Plot orientation is such that east is to the right and north is into the figure. Vector with tail denotes wind speed of 10 m s^{-1} while vector with no tail denotes wind speed between 0 and 2 m s^{-1}. 56

29. Output for control PS MCS simulation from Parker (2007) at t = 3 h. Vertical cross section of along-line averaged (from y = 250-350 km) radar reflectivity (simulated), shaded, line-parallel wind (*v,* contoured, m s^{-1}), and line-perpendicular circulation (*u* and *w* vectors, m s^{-1}). Reflectivity is only shaded for values of hydrometeor mixing ratio ≥ 1×10^{-3} g kg^{-1}. This figure is reproduced from Parker (2007). 58

30. Temperature (red), dew point (green), and frost point (blue) in degrees Celsius; and relative humidity (black) with respect to ice when $T < 0$ and with respect to liquid water when $T \geq 0$ °C from the UND Citation during the six level legs when the Nevzorov total water content was greater than 0.01 g m^{-3} on 11 May 2011. Frost point was set equal to the dew point at

temperatures greater than 0 °C. Shaded portions are during ascents, descents, and course reversals. 'East' and 'West' mark the position of the Citation at the beginning and end points of each leg. For example, the second flight leg starting at 17:13:30 traversed from west to east. 60

31. Boxplot showing variation of total water content as a function of temperature between 16:40:00 and 18:11:40 UTC on 11 May 2011. The top and bottom of a box represents the 75th and 25th percentiles, respectively, the middle line represents the median, the bottom whisker represents the smallest data point within 1.5 times the inter-quartile range (IQR)., the top whisker is the largest data point still within 1.5 times IQR, and the small circles represents data outside 1.5 times the IQR. The fifth leg was divided according to when the temperature was below 0 °C (a) and when the temperature was at or above 0 °C (b)..... 62

32. Cloud Droplet Probe (CDP) calculated liquid water content (LWC) in black and Goodrich Icing Detector Frequency (red) during the six level flight legs on 11 May 2011. 63

33. CAPPI showing radar reflectivity at 4.6 km MSL at 17:30 UTC. Black airplane symbol denotes the position of the UND Citation at 17:31 UTC..... 63

34. Boxplot showing variation of gamma intercept parameter (N_0) as a function of temperature between 16:40:00 and 18:11:40 UTC on 11 May 2011. The top and bottom of a box represents the 75th and 25th percentiles, respectively, the middle line represents the median, the bottom whisker represents the smallest data point within 1.5 times the inter-quartile range (IQR), the top whisker is the largest data point still within 1.5 times IQR, and the small circles represents data outside 1.5 times the IQR. The fifth leg is divided according to when the temperature was below 0 °C (a) and when the temperature was at or above 0 °C (b)..... 65

35. Boxplot showing variation of slope parameter (λ) as a function of temperature between 16:40:00 and 18:11:40 UTC on 11 May 2011. The top and bottom of a box represents the 75th and 25th percentiles, respectively, the middle line represents the median, the bottom whisker represents the smallest data point within 1.5 times the inter-quartile range (IQR), the top whisker is the largest data point still within 1.5 times IQR, and the small circles represents data outside 1.5 times the IQR. The fifth leg is divided according to when the temperature was below 0 °C (a) and when the temperature was at or above 0 °C (b)..... 66

36. Examples of two-dimensional cloud (2DC) probe images and mean temperature of the corresponding leg in order (top to bottom) of descending height when the Citation was at or above the melting layer on 11 May 2011. Vertical lines are timing bars. 67

37. Variation of gamma intercept parameter (N_o) with slope parameter (λ) for 10-second fits of observed number distributions between 16:40:00 and 18:11:40 UTC on 11 May 2011. Black line represents the best fit to all of the data from the six level flight legs. 69

38. Variation of gamma intercept parameter (N_0) as a function of total water content (TWC) for 10-second fits of observed number distributions between 17:13:30 and 17:20:00 UTC (second flight leg) on 11 May 2011. Black line represents the best fit to all the data from the six level flight legs. 69

39. Variation of slope parameter (λ) as a function of total water content (TWC) for 10-second fits of observed number distributions between 17:13:30 and 17:20:00 UTC (second flight leg) on 11 May 2011. Black line represents the best fit to all the data from the six level flight legs. 70

40. Variation of order of fit parameter (μ) as a function of slope parameter (λ) for 10-second fits of observed number distributions between 16:40:00 and 18:11:40 UTC on 11 May 2011. Black line represents the best fit to all the data from the six level flight legs. 70

LIST OF TABLES

Table Page

1. Sounding datasets used in the analysis of the 11 May 2011 MCS. 15

2. Sounding launch times (UTC) for locations given in Table 1 on 11 May 2011 and 00 UTC 12 May 2011. 'X' denotes a sounding launch..... 15

3. List of radars used in the analysis of the 11 May 2011 MCS (Thompson 2012, NOAA NWS Radar Operations Center 2012). NASA S-Band Transportable Dual Polarimetric Radar (NPOL) latitude and longitude information is from the position recorded in the data and the altitude is estimated based on the elevation of the ground at NPOL's position. 16

4. The NASA S-Band Transportable Dual Polarimetric Radar (NPOL) scanning strategies that were used on 11 May 2011 from 15 to 19 UTC. 17

5. Start time, end time, and altitude for the Citation II research aircraft in meters above mean sea level (MSL) and altitude for each CAPPI in meters above ground level (AGL) for the Vance Air Force Base, Oklahoma (KVNX) and the Wichita, Kansas (KICT) radars. 24

6. The total number of ten-second data points during the six level flight legs, the number and percentage of points within the range of values found by McFarquhar et al. (2007), the number and percentage above these values, and the number and percentage below. 71

7. The total number of ten-second data points during the six level flight legs that occurred when the temperature was between -10 and 0 °C, the number and percentage of points within the range of values found by McFarquhar et al. (2007), the number and percentage above these values, and the number and percentage below. 71

ACKNOWLEDGEMENTS

The author would like to thank Prof. Michael Poellot, Dr. David Delene, and Dr. Mark Askelson for serving on my thesis committee. The author would like to also thank Chris Theisen for all his help with IRIS, and the UND Citation flight crew for flying safely through challenging weather conditions.

ABSTRACT

Mesoscale convective systems (MCSs) can be classified into three organizational types: trailing stratiform (TS), leading stratiform (LS), and parallel stratiform (PS). PS type MCSs can pose challenges for forecasting as they have been shown to develop in environments favorable for discrete supercells rather than MCSs. They have also been shown to produce locally large rainfall totals due to training of convective cells, which can lead to flash flooding. While most MCS research has focused on the TS and LS types, this study focuses on understanding the PS MCS, including the microphysical variability of the stratiform precipitation region with embedded convection. During the Midlatitude Continental Convective Clouds Experiment (MC3E), a PS MCS traversed north-central Oklahoma on 11 May 2011. In-situ measurements of the stratiform precipitation region were obtained with the University of North Dakota Citation II Weather Research Aircraft in conjunction with measurements collected using a multitude of ground-based radars and a dense balloon sounding network specifically set up for the MC3E project.

At 12 UTC on 11 May 2011, there was a 300 hPa longwave trough in place over the western United States with a surface low pressure system centered over the Oklahoma panhandle. A cold front and a preceding dryline were oriented north-to-

south over western Texas. Several shortwaves at multiple levels of the atmosphere helped provide lift and overcome the strong "cap" in place over Oklahoma and northern Texas. Winds were nearly unidirectional south-southwesterly over Oklahoma and southern Kansas, which created the parallel stratiform characteristics. Line-parallel winds and line-perpendicular winds in the eastern half of the MCS were similar to a simulated PS MCS from Parker (2007). An area of westerly line-perpendicular inflow in the western half of the MCS may signal the presence of a rear-inflow jet, a feature not seen in the simulated PS MCS. A cold pool developed after the MCS took on PS characteristics.

On 11 May 2011, between 16:40 and 18:12 UTC, the Citation flew six horizontal flight legs at through the stratiform region of the PS MCS. Total water content (TWC) decreased with increasing temperature, which is similar to results McFarquhar et al. (2007) found in TS MCSs. The greatest amount of super-cooled liquid water content (LWC) was found at the end of the third flight leg, when the Citation was flying near some embedded convection in the parallel stratiform region. Gamma functions were fit to ten-second averaged two-dimensional cloud (2DC) probe spectra. N_0 and λ decreased with increasing temperature and N_0 decreased with decreasing λ, indicating aggregation was occurring in the stratiform region. Comparisons of N_0, μ, and λ with values from McFarquhar et al. (2007) show there were more small hydrometeors in the PS MCS than there were in the BAMEX trailing stratiform regions. The similarities between the 11 May 2011 PS MCS and the simulated one show that basic kinematic

features of these events are understood. This study also shows that the microphysical processes in the parallel stratiform region are similar to those in trailing stratiform regions.

CHAPTER 1: INTRODUCTION AND BACKGROUND

Classification of Mesoscale Convective Systems

A Mesoscale Convective System (MCS) is defined by Glickman (2000) as "a cloud system that occurs in connection with an ensemble of thunderstorms and produces a contiguous precipitation area ~100 km or more in horizontal scale in at least one direction." These large storms can be classified based on radar reflectivity as either linear or non-linear MCSs. Parker and Johnson (2000) define a linear MCS as an MCS "containing a convective line, by which is meant a contiguous or nearly contiguous chain of convective radar echoes that share a nearly common leading edge and move approximately in tandem, whether they are arranged in a nearly straight line or a moderately curved arc". Most MCSs also have an associated stratiform precipitation region. Linear MCSs can be classified into sub-categories based upon the orientation of the stratiform precipitation region with respect to the convective line. Parker and Johnson (2000) classified 88 linear MCSs from the months of May 1996 and May 1997 that occurred over the Great Plains of the United States into three categories: trailing stratiform (TS), leading stratiform (LS), and parallel stratiform (PS).

TS MCSs have a leading convective line with a stratiform precipitation region following behind it, as shown in Fig. 1. The defining characteristics of a TS MCS are a leading convective line that has a solid arc shape with a serrated leading edge, a very

strong reflectivity gradient along the leading edge that is generally oriented from the northeast to the southwest and is rapidly moving either eastward and/or southward, and elongated cells oriented 45-90° with respect to the whole convective line (Houze et al. 1990). The trailing stratiform region was defined by Houze et al. (1990) to be large in size with a notch-like concavity at the rear edge and a secondary maximum of reflectivity. Parker and Johnson (2000) noted that 58% of all MCSs observed in their study were classified as TS, making it the most frequently occurring type. Houze et al. (1989) observed that the front-to-rear flow in the trailing stratiform region was characterized by upward vertical motion while the rear-to-front flow was characterized by downward vertical motion.

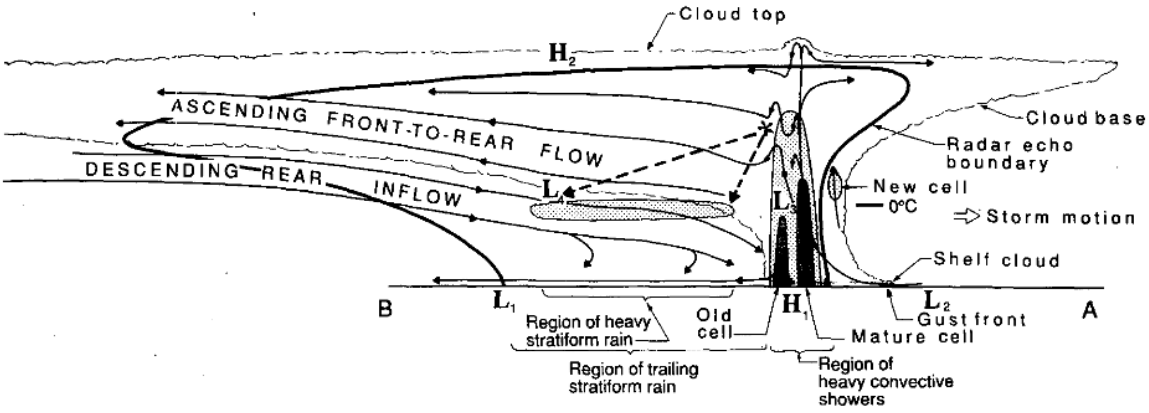

Figure 1: Conceptual model of a mesoscale convective system (MCS) with trailing stratiform (TS) region viewed in a vertical cross section oriented perpendicular to the convective line and parallel to its motion. Arrows represent storm-relative wind through the MCS. Reproduced from Houze et al. (1989).

The stratiform region can be comprised of three areas based on radar reflectivity: the transition region, the enhanced stratiform rain region, and the rear anvil region (Smith et al. 2009). The transition region is the portion of the stratiform region of lower radar reflectivities between the convective line and the enhanced stratiform rain

region. The enhanced stratiform rain region is shown in Fig. 1 as the region where heavy stratiform rain is falling to the ground and is seen as a region of a secondary reflectivity maximum. The rear anvil region is the portion of the MCS that is behind the enhanced stratiform rain region, where precipitation is evaporating before it reaches the ground.

In contrast to the TS MCS, an LS MCS is defined as "a linear MCS whose stratiform precipitation is predominately located in advance of a convective line" (Parker and Johnson 2000). LS MCSs were found to comprise about 19% of all MCSs and are divided even further into two sub-categories: front-fed LS and rear-fed LS (Parker and Johnson 2000, 2004a). Rear-fed LS systems are defined as being sustained by rear-to-front storm-relative inflow, while front-fed LS systems are sustained by lower-tropospheric storm-relative inflow flow passing through the leading stratiform precipitation region before reaching the convective line as shown in Fig. 2 (Parker and Johnson 2004a). Parker and Johnson (2000) found that front-fed was the most common type of LS MCS.

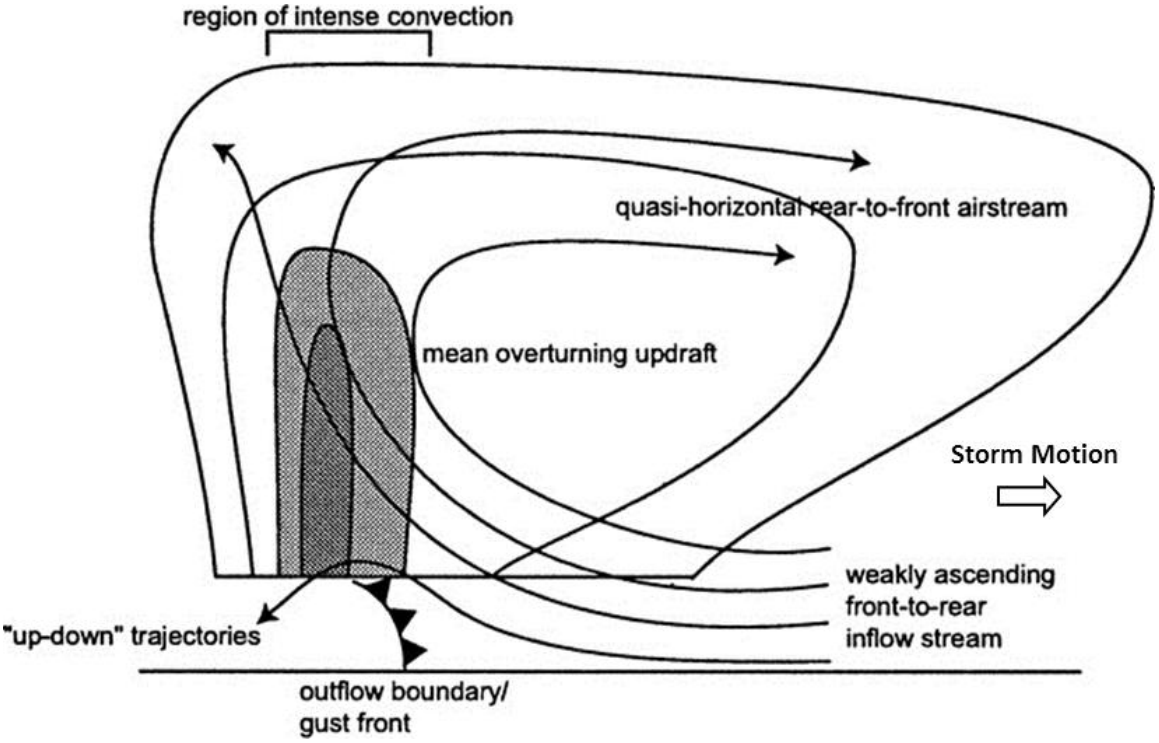

Figure 2: Conceptual model of a mesoscale convective system (MCS) with leading stratiform (LS) region based on compiled radar observations of a front-fed convective line. This vertical cross section is oriented perpendicular to the convective line and parallel to its motion. Reproduced from Parker and Johnson (2004).

Parker and Johnson (2000) classify an MCS as PS if most of the stratiform precipitation region moves parallel to the convective line and to the left of the line's motion vector, as shown in Fig. 3. PS MCSs generally have relatively large reflectivity gradients that exist on both the front and rear sides of the convective line. In PS MCSs, the front-to-rear inflow is lofted in the convective region and turns parallel to the convective line, generating the characteristic stratiform region. Parker and Johnson (2000) found that PS MCSs comprised 19% of the observed MCSs.

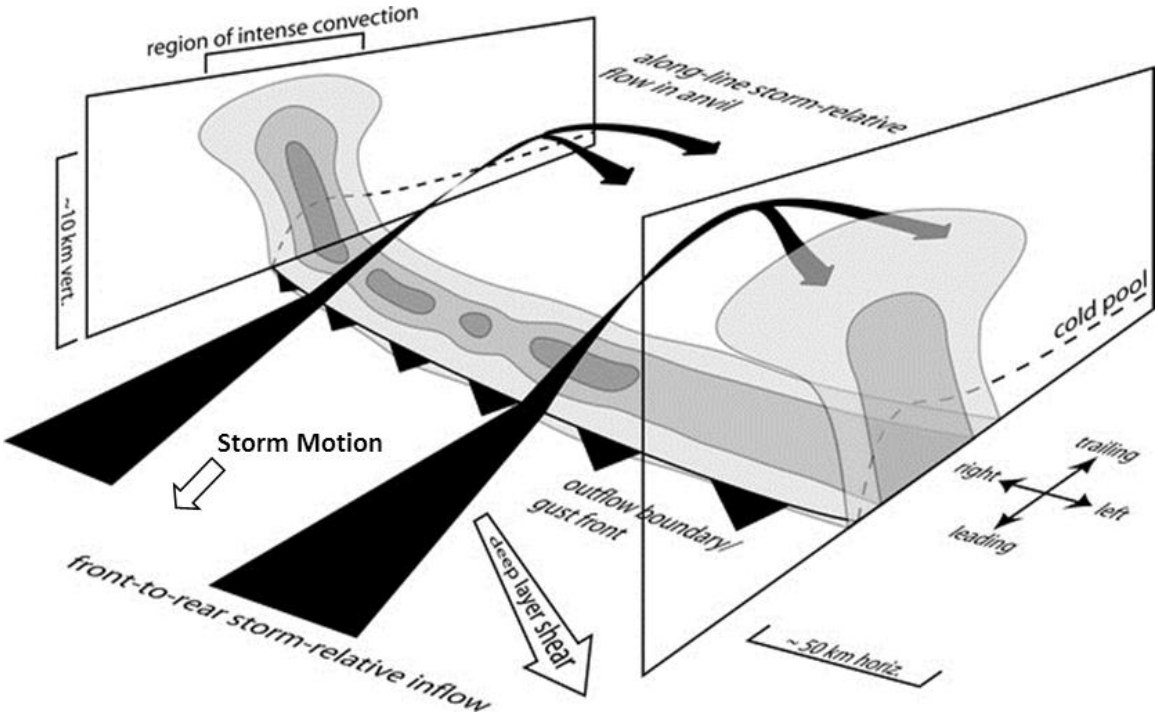

Figure 3: Conceptual model of a mesoscale convective system (MCS) with a parallel stratiform (PS) region based on compiled radar observations of a convective line. In this schematic three-dimensional rendering, the orientation of the vertical planes is perpendicular to the convective line and parallel to its motion. Reproduced from Parker (2007).

Impacts of PS MCS

PS MCSs can pose forecasting challenges due their convective type and propensity to produce severe weather. One forecasting challenge is that PS MCS occur in environments with significant deep-layer shear and clockwise-turning hodographs (Parker and Johnson 2000, Parker et al. 2001). This is a situation that is also known to favor the development of supercell thunderstorms (Moller et al. 1994). PS MCSs have also been known to produce severe weather. Gallus et al. (2008) reported that 26 (80%) of PS MCSs observed in their study produced at least one severe weather report, not including flooding reports. Large hail is a particular concern as PS MCSs each produced

on average between five and six reports of hail having diameters between 1 and 2 inches. Of these, there were an average 0.5 reports of hail having diameters greater than 2 inches, the most of any type of storm analyzed including supercells. Gallus et al. (2008) also reported an average of 1.6 tornadoes per each PS MCS, the most for any type of MCS.

Another concern with PS MCSs is flooding potential. Schumacher and Johnson (2005) found that 9.2% of MCSs observed were classified as PS MCS during the time they produced extreme rainfall, which contributed to 6.0% of all events that produced extreme rainfall. Gallus et al. (2008) reported that PS MCSs had 3.5 reports per PS MCS of any kind of flooding and produced 8% of the total flooding reports. The reason that PS MCSs produce significant flooding is they often advect convective echoes parallel to the convective line and over the same locations (Parker and Johnson 2000, Schumacher and Johnson 2005).

Past Research on Trailing Stratiform (TS) and Leading Stratiform (LS) Mesoscale Convective Systems (MCSs)

From 20 May to 6 July 2003, the Bow Echo and Mesoscale Convective Vortex Experiment (BAMEX) was conducted over the central United States, and 26 MCSs were sampled during this experiment (Davis, et al. 2004). The National Oceanic and Atmospheric Administration (NOAA) P-3 Research Aircraft was flown in 17 in-situ spiral descents in which temperatures ranged from −10 to +10 °C, with microphysical instruments and a radar onboard to sample the vertical microphysical structure of MCS

stratiform regions (Davis et al. 2004, McFarquhar et al. 2007). While most of the sampled MCSs were of the TS type, on 31 May 2003 a front-fed LS MCS was sampled and on 22 June 2003 an MCS with PS characteristics was sampled (Storm et al. 2007, Halligan and Parker 2004).

McFarquhar et al. (2007) investigated the microphysical properties of the TS and LS MCSs observed during the BAMEX field campaign, but did not study the 22 June 2003 PS MCS. For all but one of the analyzed spiral descents, the environment above the 0 °C isotherm was at or near saturation with respect to ice. McFarquhar et al. (2007) also found the relative humidity with respect to liquid water below the melting layer decreased by 3% $°C^{-1}$. The total mass content (TMC) in the BAMEX stratiform regions was on average 1.44 ± 0.89 g m^{-3} (McFarquhar et al. 2007). Averaged over all spirals, the total hydrometeor number concentration (N_t) decreased at a rate of 19% ± 10% $°C^{-1}$ (i.e. N_0 decreased with increasing temperature) and the TMC decreased by 10% ± 7% $°C^{-1}$. The faster decrease in the total number concentration than TMC was thought to be a result of aggregation and sublimation occurring in the stratiform region.

McFarquhar et al. (2007) fit a gamma distribution to size distributions of hydrometeors averaged over 60 seconds and observed in 16 spiral descents in both TS and LS MCSs in BAMEX. The gamma function is given by

$$N(D) = N_0 D^{\mu} \exp(-\lambda D), \quad (1)$$

where $N(D)$ is the number concentration of particles at diameter D, N_0 is the intercept parameter, μ is the order of fit, and λ is the slope parameter. Chi-squared (χ^2) fits based

on the total number of particles were used as the measure of the goodness-of-fit and a nonlinear Levenberg-Marquardt technique was used to minimize the χ^2 fits. McFarquhar et al. (2007) found that the slope parameter λ ranged between 0 and 20 cm^{-1}, N_0 ranged between 10^{-4} and 10^{-1} $cm^{-(3+\mu)}$ μm^{-1}, and μ ranged from -2 and 0 for BAMEX stratiform regions above the melting layer. Aggregation was occurring in the stratiform regions due to the fact that λ decreased with increasing temperature and that *N(D)* decreased with respect to increasing temperature for particle diameters less than 2 mm (McFarquhar et al. 2007).

Smith et al. (2009) analyzed ten-second averaged data from 12 spiral descents and five horizontal flight legs to characterize the trailing stratiform region of BAMEX MCSs. Within the enhanced precipitation region of the TS MCS, conditions were saturated with respect to ice above and within the melting layer. The steady decrease of N_t and λ from the top of the spirals to the bottom of the melting layer indicated that aggregation was occurring and that sublimation was insignificant. Smith et al. (2009) also found that some areas of the rear anvil region were saturated with respect to ice above the base of the anvil, but that other areas were significantly subsaturated. Smith et al. (2009) concluded that sublimation was occurring in the rear anvil region in addition to aggregation due to the fact that N_t had a steeper rate of decrease with respect to increasing temperature than it did in the enhanced stratiform rain region.

Past Research on Parallel-Stratiform Type Mesoscale Convective Systems

It has been found that the characteristic shape of PS-type MCSs is the result of wind flow around and through the storm. PS MCSs have modest rear-to-front storm-relative winds at upper levels, weak line-perpendicular middle-tropospheric storm-relative winds, and greater line perpendicular flow in the 0-1 km layer than TS MCSs (Parker and Johnson 2000). Parker (2007) observed that lower-tropospheric advection and outflow expansion to the right of the convective line (relative to the storm motion vector in Fig. 3) produces back-building, generating new convection. At the same time, upper-tropospheric storm-relative hydrometeor advection towards the left of the convective line (relative to the storm motion vector in Fig. 3) produces a line-parallel precipitation region (Parker 2007).

Parker (2007) found that convective regions of PS MCSs produce most of their outflow in close proximity to the surface outflow boundary, leading to the rapid development of boundary layer cold pools. Strengthening cold pools lead to deeper cold pools, providing deeper lifting along the main north-south outflow boundary. Halligan and Parker (2004) observed that the PS MCS was unlikely to remain a PS type because the low-level line-perpendicular shear was not sufficient to balance the strengthening cold pool. Parker and Johnson (2000) found that 58% of all PS MCSs eventually evolved into a TS MCS, and PS MCSs with large line-parallel shear are able to retain PS structure the longest before becoming TS.

Overview of the Midlatitude Continental Convective Clouds Experiment (MC3E)

The Midlatitude Continental Convective Clouds Experiment (MC3E) was conducted from 22 April to 6 June 2011 in Oklahoma (Petersen and Jensen 2012). The experiment was a joint project between the U.S. Department of Energy (DOE) Atmospheric Radiation Measurement (ARM) Climate Research Facility and NASA Global Precipitation Measurement (GPM) mission Ground Validation program (Jensen et al. 2010). The overarching goal of MC3E is to "provide the most complete characterization of convective cloud systems, precipitation, and the environment that has ever been obtained…" (Jensen et al. 2010).

During MC3E, a wide variety of ground-based and airborne instruments were used to collect observations of convective storms and their environments. Ground precipitation amount and rain drop size distributions were measured using a surface network of over 20 disdrometers and rain gauges (Petersen and Jensen 2012). Seven different ground-based multi-frequency cloud and precipitation dual-polarimetric radars covering the W, Ka, Ku, X, C, and S bands were used to observe cloud and precipitation events (Jensen et al. 2010). These ground measurements were augmented with a six-station rawinsonde network within which soundings were launched four to eight times a day (Jensen et al. 2010). Sampling the clouds from above, the NASA ER-2 aircraft carried the HIWRAP Ka-Ku band radar and the AMPR and CosMIR radiometers, which measured upwelling radiation in the range from 10 to 183 GHz (Petersen and Jensen 2012). In-situ cloud measurements were collected using a suite of instruments on board the

University of North Dakota (UND) Citation II Weather Research Aircraft (referred to as the Citation for the rest of this paper).

On 11 May 2011, a PS MCS traversed north-central Oklahoma. In-situ measurements of the stratiform precipitation region were obtained with the Citation in conjunction with measurements collected using the multitude of ground-based radars and the dense rawinsonde network. From 16:50 to 18:10 UTC, the six horizontal flight legs were flown by the Citation at approximately 7500 m, 6600 m, 5600 m, 4700 m, 3700 m, and 2800 m above mean sea level (MSL).

The purpose herein is to conduct a detailed case study of the 11 May PS MCS from MC3E. The synoptic and mesoscale environments are derived from satellite, radar, and sounding data. A detailed microphysical analysis of the parallel stratiform region is also performed using data collected with the Citation. Results of this study should help improve the accuracy of operational and research numerical models as well as provide more insight into PS MCSs.

CHAPTER 2: DATA

Synoptic Analysis Data

Upper-air synoptic scale constant pressure objective analysis charts at the 925, 850, 700, 500, 300, and 250 hPa constant pressure levels were obtained from the Storm Prediction Center (SPC) Surface and Upper Air archive website (http://www.spc.noaa.gov/obswx/maps) and from the Plymouth State Weather Center website (http://vortex.plymouth.edu/u-make.html). Surface pressure and frontal analysis charts were obtained from the Unisys Weather Image and Map Archive (http://weather.unisys.com/archive).

Mesoscale Analysis Data

Archived SPC mesoscale analysis graphics, which are generated from the merging of objective surface analyses with Rapid Update Cycle (RUC) model upper-air analyses and produce three-dimensional atmospheric analyses, are available from http://www.spc.noaa.gov/exper/ma_archive (Storm Prediction Center 2012). In these analyses, many additional parameters such as potential temperature, frontogenesis, precipitable water, etc. are calculated at each grid point. The 300 hPa constant pressure chart and the surface-based convective available potential energy (CAPE) chart are used to analyze the mesoscale environment.

Regional visible and infrared satellite images were obtained from the National Center for Atmospheric Research (NCAR) image archive website (http://www.mmm.ucar.edu/imagearchive). The 1 km resolution satellite images were centered over Wichita, Kansas, and were available every 30 minutes. The area covered extended from northern Nebraska to central Texas, and from central Colorado to western Illinois. Regional National Weather Service (NWS) Weather Surveillance Radar 88 Doppler (WSR-88D) radar reflectivity mosaic imagery was also obtained from the NCAR image archive website. The coverage of the radar imagery was similar to that of the satellite imagery, but extended further north into southern South Dakota and not as far south into Texas. The western extent of the imagery was also increased to include the eastern two-thirds of Colorado. Hourly surface temperature charts and surface station meteograms from 11 May were obtained from the Plymouth State Weather Center website (http://vortex.plymouth.edu/u-make.html). Meteograms were obtained for Ponca City, Enid, and Stillwater (all in Oklahoma).

Sounding Data

Sounding data were obtained from two sources: ARM and the NWS. Balloon-borne rawinsondes were launched from the SGP Central Facility as well as from five outer launching sites distributed around southern Kansas and northern Oklahoma (shown in Fig. 4). Table 1 provides location information for the six ARM and four NWS sounding sites used in this study. Data from the five outer sounding launch sites were obtained from the ARM website (http://iop.archive.arm.gov/arm-

iop/2011/sgp/mc3e/jensen-sonde), while sounding data from the Central ARM Facility were obtained through the ARM data archive website (http://www.arm.gov/data/datastreams/sondewnpn). The NWS sounding data were obtained from the University of Wyoming atmospheric soundings website (http://weather.uwyo.edu/upperair/sounding.html). Table 2 lists the times and locations for soundings collected on 11 May.

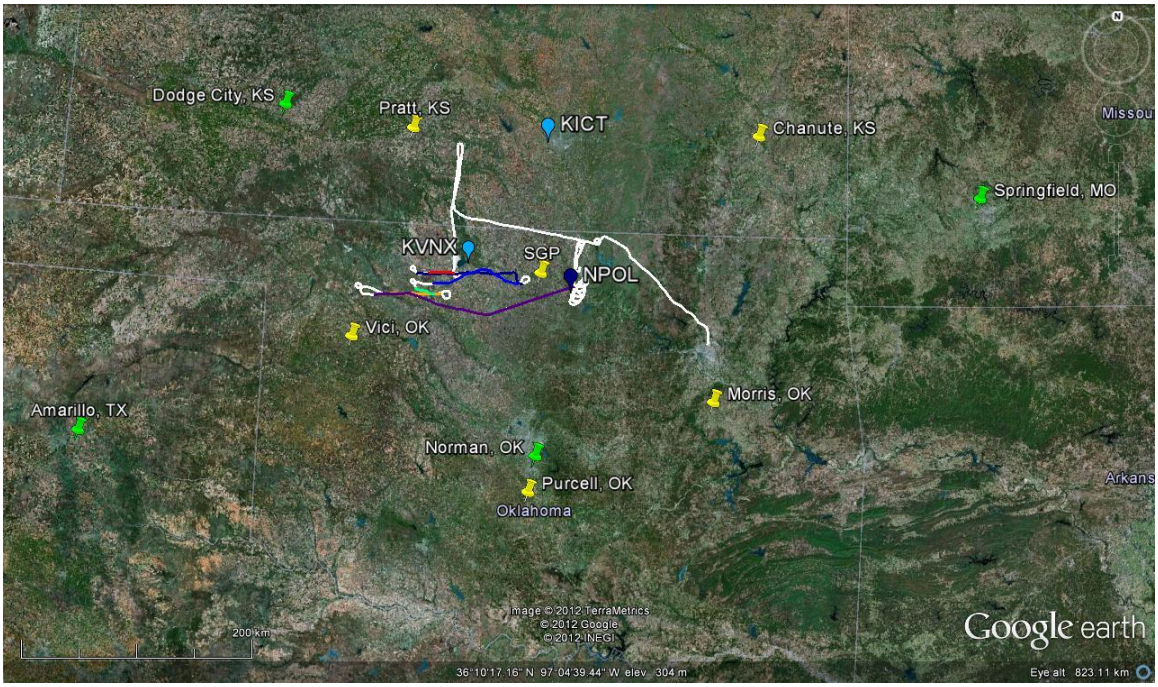

Figure 4: Map of National Weather Service (NWS) sounding launch sites (green push pins), Department of Energy (DOE) Atmospheric Radiation Measurement (ARM) sounding launch sites (yellow push pins), NWS Weather Surveillance Radars 88-Doppler (WSR-88D) locations (green balloons), and NASA S-Band Transportable Dual Polarimetric Radar (NPOL) location (blue balloon). The multi-colored line depicts the Citation flight track on 11 May 2011.

Table 1: Sounding datasets used in the analysis of the 11 May 2011 MCS.

Site ID	Nearest Town	State	Latitude (°N)	Longitude (°W)
SGP	SGP Central Facility	Oklahoma	36.61	97.49
S01	Pratt	Kansas	37.64	98.75
S02	Chanute	Kansas	37.67	95.49
S03	Vici	Oklahoma	36.07	99.20
S04	Morris	Oklahoma	35.69	95.86
S05	Purcell	Oklahoma	34.98	97.52
KAMA	Amarillo	Texas	35.22	101.70
KDDC	Dodge City	Kansas	37.77	99.97
KOUN	Norman	Oklahoma	35.25	97.47
KSGF	Springfield	Missouri	37.23	93.38

Table 2: Sounding launch times (UTC) for locations given in Table 1 on 11 May 2011 and 00 UTC 12 May 2011. 'X' denotes a sounding launch.

Site ID	00	03	06	09	12	15	18	21	00 UTC 12 May
SGP	X	X	X	X	X	X	X		
S01	X	X	X	X	X	X	X	X	X
S02	X	X	X	X	X	X	X	X	X
S03	X	X	X		X	X	X	X	X
S04	X	X	X	X	X	X		X	
S05	X	X	X	X	X	X		X	X
KAMA					X				X
KDDC	X				X				X
KOUN	X				X				X
KSGF	X				X				X

Doppler Radar Data

Overview of the Doppler radar coverage

During MC3E, an array of radars operating at a variety of wavelengths were used to sample cloud and precipitation processes. ARM operated four precipitation radars and several cloud radars at and around the SGP Central Facility. The NASA S-Band Transportable Dual Polarimetric Radar (NPOL) was brought in to augment the array of ARM research radars. The radar data were primarily used to obtain radar radial velocity

measurements; hence the S-Band radars were used instead of the shorter wavelength radars since the S-Band radars have larger Nyquist velocities.

National Weather Service (NWS) Radars

Two NWS WSR-88D radars in and near the MC3E domain were used. The NWS radar data were procured from the National Climatic data center website (http://www.ncdc.noaa.gov/nexradinv). Data from the Vance Air Force Base (KVNX) and the Wichita, Kansas (KICT), radars for the period from 16:40 to 18:20 UTC on 11 May, 2011 were used (Table 3; these radars are also shown in Fig. 4). While the MCS was over the MC3E research area, these radars were being used to collect 360° volume scans having 14 elevations between 0.5° and 19.6°.

Table 3: List of radars used in the analysis of the 11 May 2011 MCS (Thompson 2012, NOAA NWS Radar Operations Center 2012). NASA S-Band Transportable Dual Polarimetric Radar (NPOL) latitude and longitude information is from the position recorded in the data and the altitude is estimated based on the elevation of the ground at NPOL's position.

Radar	Latitude (°N)	Longitude (°W)	Altitude (m MSL)
Vance AFB	36.74	98.12	369
Wichita	37.65	97.43	407
NPOL	36.5	97.2	300 (est.)

NPOL Radar

NPOL was deployed "to provide dual-polarimetric measurements of light to heavy precipitation in liquid, mixed, and ice phase environments" (Jensen et al. 2010). Several scanning modes were used with NPOL during the time the Citation was sampling the MCS, which are summarized in Table 4. NPOL data were obtained from the NASA

data archives at ftp://gpm.nsstc.nasa.gov/gpm_validation/mc3e/NPOL/data. Data from the 270° azimuth RHI scans from 17:00 UTC to 18:15 UTC were used to determine the east-west component of the horizontal wind field.

Table 4: The NASA S-Band Transportable Dual Polarimetric Radar (NPOL) scanning strategies that were used on 11 May 2011 from 15 to 19 UTC.

Start Time (UTC)	Scan
15:00	360° Volume scan from 0.484° to 13.5° elevations
16:18	RHI scan from 257° to 262° azimuths
17:00	RHI scan from 265° to 270° azimuths
17:27	RHI scan from 270° to 275° azimuths
18:15	RHI scan from 328° to 333° azimuths
18:26	260° to 350° azimuths sector scan from 0.484° to 13.5° elevations

Citation Microphysical Data

All data collected from the Citation were processed using the Airborne Data Processing and Analysis (ADPAA) package (Delene 2011). All data that were measured at a higher frequency than once per second were averaged into 1 Hz data.

State Parameter Instrumentation

Total temperature[1] data were obtained with the Rosemount Platinum Resistance total temperature sensor and were corrected for compressional heating and aerodynamic influences during flight to obtain atmospheric ambient temperature (Stickney et al. 1981). A tunable diode laser (TDL) hygrometer was used to measure the water vapor mixing ratio (May 1998). These measurements were converted into dew

[1] Total temperature is defined as the maximum air temperature which can be attained by 100% conversion of the kinetic energy of the flight [via adiabatic compression into internal energy and adding this to the ambient air temperature] (Stickney et al. 1981).

point, frost point, and relative humidity using the Airborne Data Processing and Analysis program (Delene 2011). Atmospheric pressure was measured using an absolute pressure transducer connected to a static pressure port on the side of the Citation aircraft.

Liquid and Total Water Sensors

The Sky Tech Research Nevzorov probe was used to measure liquid water content (LWC) and total water content (TWC) (Korolev et al. 1998). Both LWC and TWC are obtained with this probe using "hotwire" sensors. LWC is measured using a hotwire coiled around a bar and attached to both the front (collector) and the back (reference) of the instrument. The difference between the current needed to maintain a constant temperature on the collector and reference hotwire sensors is proportional to the amount of liquid water evaporating off of the collector sensor. The TWC sensor works much the same way, with the exception that the leading TWC hotwire sensor is wrapped around the inside of a cone. This cone collects both liquid and solid particles, which are vaporized. The Nevzorov probe used in this project was a "deep cone" model, which suffers less particle bounce and consequently has better collection efficiency than older models. The heated wire in the collection cone can be overwhelmed in high water content conditions. Thus, while the stated range of TWC and LWC values is 0.003 to 3 g m^{-3}, the TWC values appeared to saturate around 1.5 g m^{-3}. The corresponding TWC reference is a coil wrapped around the outside of the back of the cone away from most precipitation and air stream influences.

Gust Probe and Wind Measurements

Three-dimensional wind is calculated from measurements collected with a gust probe in combination with an Applanix Position and Orientation System (POS). A 5-port gust probe is mounted on a boom in front of the aircraft's nose. This probe is used to determine the flow of air relative to the aircraft. The center port (Pitot) is connected to a differential pressure transducer and provides a measurement of the difference in the ram air pressure to the ambient air pressure, which is used to calculate the indicated air speed of the aircraft. The true air speed (TAS) of the aircraft is derived from the indicated air speed corrected for temperature and ambient pressure. The ports above and below the center port are connected to another differential pressure transducer and are used to measure the angle of the Citation relative to a horizontal plane. The ports to the left and right of the center port are connected to a third differential pressure transducer and provide a measurement of the sideslip angle of the Citation relative to the airflow. An additional Pitot sensor located on the left wing of the aircraft is used to measure indicated air speed. Since the Pitot port in the flow angle probe tends to get plugged in regions of high ice hydrometeor mass concentrations, the wing Pitot measurement was used as the primary source of indicated air speed.

The Applanix Position and Orientation system provides measurements of the three-dimensional GPS position of the aircraft using a GPS receiver as well as three-dimensional aircraft accelerations measured with an Inertial Measurement Unit (IMU). The IMU, described in Mostafa et al. (2001), is comprised of triads of accelerometers

and gyros that measure three-dimensional accelerations and aircraft orientation. The POS control computer integrates IMU measurements in a "strapdown" inertial navigator to produce the position, velocity, and orientation of the IMU relative to the Earth. GPS data are integrated into the data provided by the IMU to correct for drift in the accelerometer and gyro measurements that occur over time.

The POS provides aircraft orientation and motion in an Earth-relative coordinate system. Lenschow (1986) describes the method for deriving three-dimensional winds from aircraft-relative flow and the motion of the aircraft relative to the ground (Delene 2012).

Two-Dimensional Cloud Probe

The two-dimensional cloud (2DC) probe was manufactured by Particle Measuring Systems, Inc., and has an effective spacing of 30 μm per sensing diode with 32 diodes in the array, giving a maximum image width of 960 μm. Prior to MC3E, the standard 2DC tips were replaced with new Korolev tips which have been shown to reduce the number of data artifacts due to shattered particles (Korolev 2011).

The 2DC image data were processed and binned into 24 bins based on diameter. The processing was performed at UND using algorithms based on Heymsfield and Parrish (1978). Particles are rejected if:

- the area ratio is less than 0.1,
- the area ratio is less than 0.2 and the size is greater than twenty times the resolution of the probe (600 μm),

- the entire particle buffer area is solid,
- the entire particle buffer area is zero.

The area ratio is the ratio of the particle area to the area of an equivalently sized circle. Particles are reconstructed using the "center-in" reconstruction method described in Heymsfield and Parrish (1978). This method fits a circle to the shadowed area of each particle that passes the rejection criteria. It also reconstructs partially sampled particles at the edges of the array, although if the center of the particle is not recorded, the particle size will be computed to be smaller than it actually was.

There are several sources of uncertainty with 2DC measurements. The first area of uncertainty is that associated with the calculation of all concentrations and hydrometeor sizes. Gayet et al. (2004) stated that the uncertainty for concentration is ±50% and for size is ±25%. Another area of uncertainty arises owing to shattered particles. Artificially high concentrations of small hydrometeors can be created when a real hydrometeor impacts the 2DC, shatters into several, smaller hydrometeors, and then these artificial hydrometeors are sampled by the 2DC. Hydrometeor shattering adds additional uncertainty to the 2DC measurements to what was stated in Gayet et al. (2004). Korolev tips help reduce this uncertainty by redirecting shattered hydrometeors away from the sampling area. Quality control checks in the processing software also help reduce this uncertainty. Another uncertainty arises in the computation of the average number concentration for larger particles. Very few large hydrometeors are present compared to small hydrometeors, so even in a ten-second sample, there may not always be enough large hydrometeors to produce a representative value.

CHAPTER 3: METHODOLOGY

The analysis techniques described in this chapter are a combination of visual and numerical analysis. The upper-air charts were visually analyzed to determine the synoptic and mesoscale environment on 11 May. The surface charts were visually analyzed for the development of a cold pool. The sounding and microphysical data are processed using the methodology given in this chapter and then are analyzed for characteristics and trends.

Sounding Analysis

The ARM sounding data have been archived into netCDF format and the NWS sounding data were stored in an ASCII text file. Both sets of sounding data are converted into the FSL Rawinsonde data format (NOAA 2012), and are subsequently plotted with the Universal RAwinsonde Observation (RAOB) program. The RAOB program was used to create Skew-T/Log-P thermodynamic diagrams along with a vertical profile of the winds and simple hodographs. A problem with RAOB was that it does not plot all of the observed wind levels in the ARM soundings. To see the entire vertical wind profile for each of the soundings, a custom script was created to plot each wind measurement in the sounding and classify it according to wind speed.

Another script was created to overlay the temperature, dew point, and wind observation at a single pressure level onto a map of Oklahoma and portions of adjacent states. The script created an image for the mandatory pressure levels 1000 hPa, 925 hPa, 850 hPa, 700 hPa, 500 hPa, 300 hPa, 250 hPa, 200 hPa, and 100 hPa for all the sounding data available at the sounding launch times listed in Table 2. Temperature, dew point, wind speed, and wind direction observations from the Citation data are added to the 15 UTC chart.

Doppler Radar Velocity Analysis

Level II radar data from Wichita, Kansas (KICT) and Vance Air Force Base, Oklahoma (KVNX) are converted to Universal Format using software called Radar2uf, developed at UND by Paul Kucera in 1999. The Vaisala Sigmet Interactive Radar and Information Software (IRIS) is used to visualize the data (Vaisala 2009). Radial wind velocities measured by the radars are plotted on constant altitude PPIs (CAPPIs). The altitudes of the CAPPIs are at the same altitude above sea level as the Citation while it flew level flight legs through the stratiform region of the MCS (Table 5). The CAPPIs are visually analyzed to determine the wind flow pattern through the MCS.

NPOL radial velocity data are also used to estimate wind direction and speed in the MCS. Relative Height Indicator (RHI) plots along a selected azimuth are created using the Unidata Integrated Data Viewer. The 270° azimuth RHI is chosen because it would give an indication of the east-west component of the horizontal wind and was located in the sector scan that covered the Citation's sampling area.

Table 5: Start time, end time, and altitude for the Citation II Research Aircraft in meters above mean sea level (MSL) and altitude for each CAPPI in meters above ground level (AGL) for the Vance Air Force Base, Oklahoma (KVNX) and the Wichita, Kansas (KICT) radars.

Leg	Start Time (UTC)	End Time (UTC)	Citation altitude (m MSL)	KVNX CAPPI altitude (m AGL)	KICT CAPPI altitude (m AGL)
1	16:40:00	17:06:40	7530	7160	7130
2	17:13:30	17:20:00	6590	6220	6180
3	17:24:10	17:27:30	5630	5260	4220
4	17:31:40	17:44:00	4710	4340	4300
5	17:47:10	18:03:10	3730	3360	3320
6	18:07:30	18:11:40	2780	2410	2380

Citation Microphysical Data Analysis

The Citation level flight legs are determined by subjectively analyzing the Citation altitude time series data. The Citation altitude data are plotted against time for the entire flight and flight segments with minimal changes in altitude were chosen for analysis. The in-cloud portion of each flight leg, as defined by Nevzorov TWC greater than 0.01 g m^{-3}, was characterized by the following parameters: altitude, pressure, temperature, dew point or frost point, relative humidity with respect to ice and/or liquid water, total water content, and liquid water content. Time series of these data are plotted and in-cloud statistics of each variable for each flight leg are calculated using the Airborne Data Processing and Analysis Cplot program (Delene 2011).

In addition to a statistical characterization, ten-second averaged gamma distributions are fit to the 2DC spectral data as follows. The 1 Hz spectral data are

normalized with respect to bin width and averaged into ten-second intervals. The data are normalized with the following formula:

$$N(D) = \frac{N_u(D)}{D_{e1} - D_{e0}} \quad (2)$$

where *N(D)* is the normalized number concentration in the bin with mean diameter *D*, $N_u(D)$ is the un-normalized number concentration, D_{e1} is the diameter defining the upper limit of the bin, and D_{e0} is the diameter defining the lower limit of the bin.

All 1 Hz spectra containing missing value code are discarded and only ten-second averaged spectra with a total concentration greater than $1*10^{-11}$ cm^{-3} are discarded are considered valid. The gamma function given in Eq. 1 is fit to the ten-second averaged spectrum using a Levenberg-Marquardt fitting technique (Press et al. 1992).

The Levenberg-Marquardt technique is a numerical method that minimizes a given function by smoothly varying between two different minimization optimization methods: the steepest descent method and the inverse-Hessian method. The steepest descent method is used when the current solution is far from the minimum and the inverse-Hessian method is used when the current solution is close to the minimum. The function that is minimized was a chi-squared (χ^2) function given by

$$\chi^2 = \frac{\sum_{i=1}^{n} \left[N_f(D_i) - N_{obs}(D_i)\right]^2}{n-1} \quad (3)$$

where N_f is number concentration of hydrometers with diameter D_i of the fitted distribution, N_{obs} is the observed number concentration of hydrometeors with diameter D_i, and *n* is the number of bins in the observed spectrum.

The ten-second averaged spectra are fit to three types of distributions: the gamma function given in Eq. 1 fit over the entire spectrum, a gamma function set over the entire spectrum where μ is set to zero (an exponential function), and a bimodal gamma distribution. For each new gamma distribution fit, the smallest χ^2 value is saved. The fit with the smallest χ^2 value among the three function fits is used as the fit for the spectrum.

To create a bimodal fit, each spectrum is tested for bimodality based on the method described in Mace et al. (2002). A spectrum is bimodal if the decrease in slope is more than 25% of the slope between the next highest and lowest bins. If the spectrum is bimodal, the spectrum is split at the bin where bimodality is detected and gamma functions are fitted to both parts of the spectrum. Only two modes are assumed to be present in any individual spectrum. If both parts of the bimodal spectrum have a valid gamma fit, the χ^2 values for each part are averaged to create a combined χ^2. Otherwise, the χ^2 value for the part of the distribution that did have a valid fit was used for the whole spectrum.

Figure 5 shows an example of when both μ and λ are greater than zero. Figure 6 shows an example of a function with μ less than zero. The negative μ gives the gamma function a larger negative slope than it would have for a positive μ. An example of Figure 7 shows an example of a spectrum that was fitted with a piecewise function for a bimodal spectrum and is also an example of when both μ and λ are negative. This function is similar to the one shown in Fig.6, but the negative λ changes the slope of the gamma function at the largest drop diameters. If this function were extended out to

even larger drop diameters, the gamma function would start to increase with increasing drop diameter.

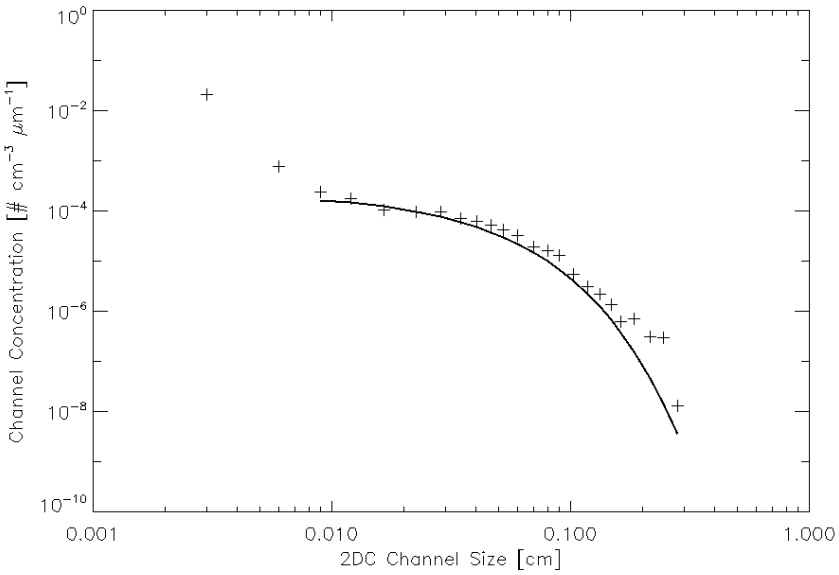

Figure 5: Sample ten-second spectrum from 17:17:29 UTC on 11 May 2011 showing a fitted gamma function that has a positive μ and a positive λ. The solid line is the function $N(D)=2.41*10^{-4}*D^{0.00727}*\exp(-39.7*D)$.

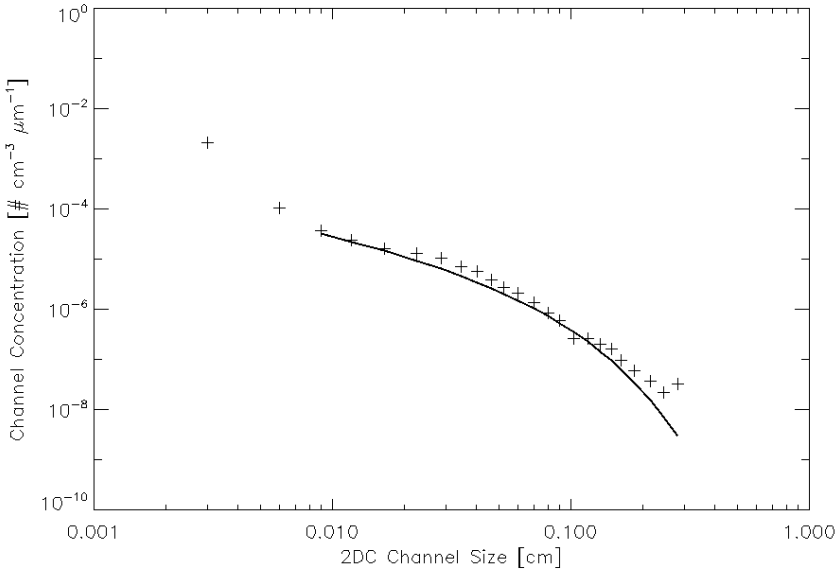

Figure 6: Sample ten-second spectrum from 17:16:49 UTC on 11 May 2011 showing a fitted gamma function that has a negative μ and positive λ. Solid line is the function $N(D)=2.72*10^{-7}*D^{-1.05}*\exp(-20.9*D)$.

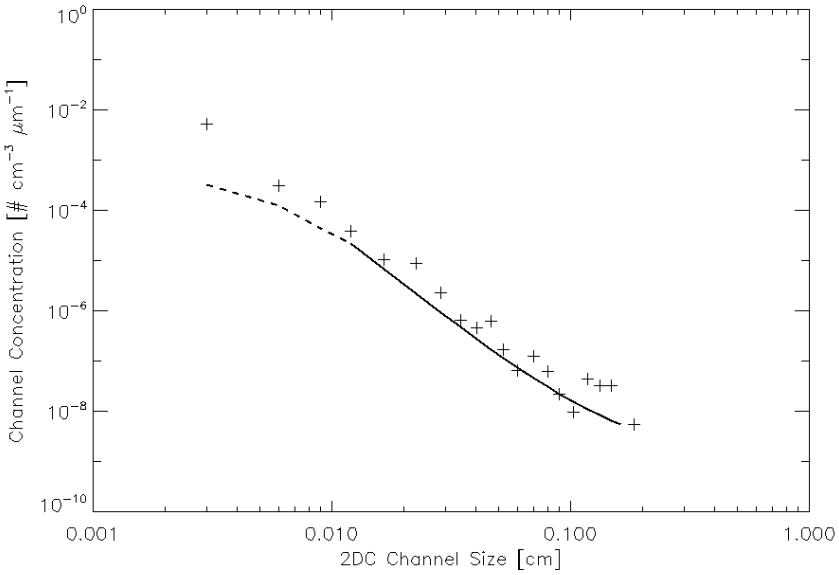

Figure 7: Sample ten-second spectrum from 16:52:09 UTC on 11 May 2011 showing a bimodal spectrum with two fitted gamma functions. The first fitted function has a positive μ and a positive λ and the second fitted function has a negative μ and a negative λ. The combined function fit is represented by: $N(D)=5.23*10^{-3}*D^{0.282}*\exp(-385*D)$ when D <= 120 µm (dashed line) and $N(D)=5.72*10^{-13}*D^{-3.92}*\exp(12.5*D)$ when D > 120 µm (solid line).

Quality assurance checks are run on the fitted gamma distributions. Fitted gamma distributions are discarded if N_0 is either less than 0 $cm^{-(3+\mu)}$ μm^{-1} or greater than 1000 $cm^{-(3+\mu)}$ μm^{-1}; if μ is less than -100 or greater than 1000; or if λ is less than -40 cm^{-1} or greater than 100 cm^{-1}. These limits are based on a subjective analysis of the data and are determined to be the bounds of a representative fit. Values of λ greater than 100 cm^{-1} cause the gamma functions to predict very small number concentrations for the bins with the largest diameters in the spectrum (Fig. 8). This is not representative of the actual spectra and thus should be discarded. This pattern is similar in all spectra in which the λ from the second gamma function is greater than 100 cm^{-1}, thus functions with λ greater than 100 cm^{-1} are discarded.

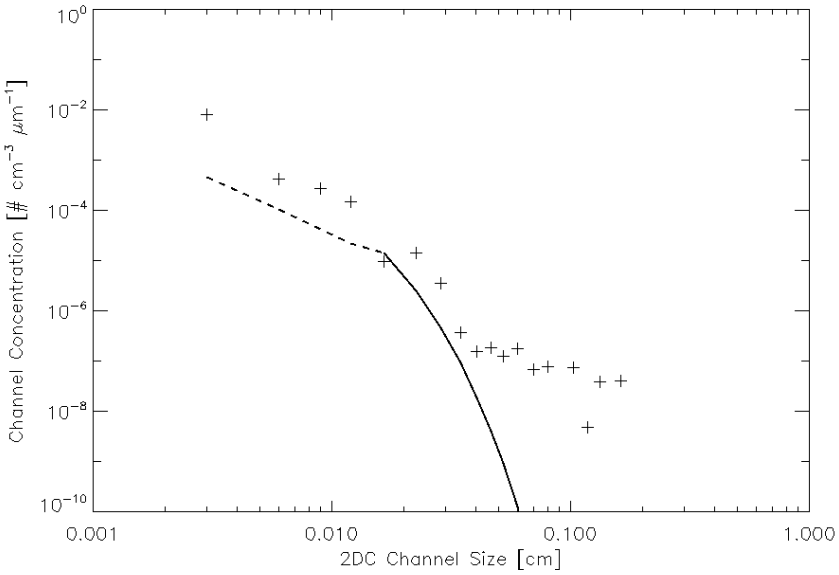

Figure 8: Sample ten-second spectrum from 16:51:39 UTC showing a bimodal spectrum with the second gamma function having a λ greater than 100 cm^{-1}. The combined function fit is represented by: N(D)=4.09*10^{-9}*D$^{-2.01}$*exp(-27.2*D) when D <= 225 µm (dashed line) and N(D)=6.47*10^{-6}*D$^{-1.13}$*exp(234*D) when D > 225 µm (solid line).

CHAPTER 4: RESULTS AND DISCUSSION

In this chapter the synoptic, mesoscale, and thermodynamic environment in which the PS MCS developed are presented. The wind flow pattern in and around the MCS as determined from sounding, radar, and in-situ measurements will be shown. This chapter will conclude by showing the microphysical characteristics of the parallel stratiform region.

Synoptic, Mesoscale, and Thermodynamic Environment

On 11 May 2011 at 12 UTC, a longwave ridge was present over the eastern half of the contiguous United States with a longwave trough over the western half as shown in Fig. 9. The jet stream on the east side of the longwave trough extended from southern New Mexico at the base of the trough northeastward through the Great Plains and into North Dakota. Figure 9 also shows a jet streak embedded in the jet stream over eastern Colorado. The right entrance region of this jet streak is located over southeastern Colorado and is an area of upper-level divergence. There is also a region of faster wind speeds extending from eastern Colorado to southeastern Kansas, indicating that just south of this feature the wind speeds will be accelerating and creating another area of upper-level divergence. From the continuity equation, both of

these areas of upper-level divergence would create and/or support areas of rising vertical air motion.

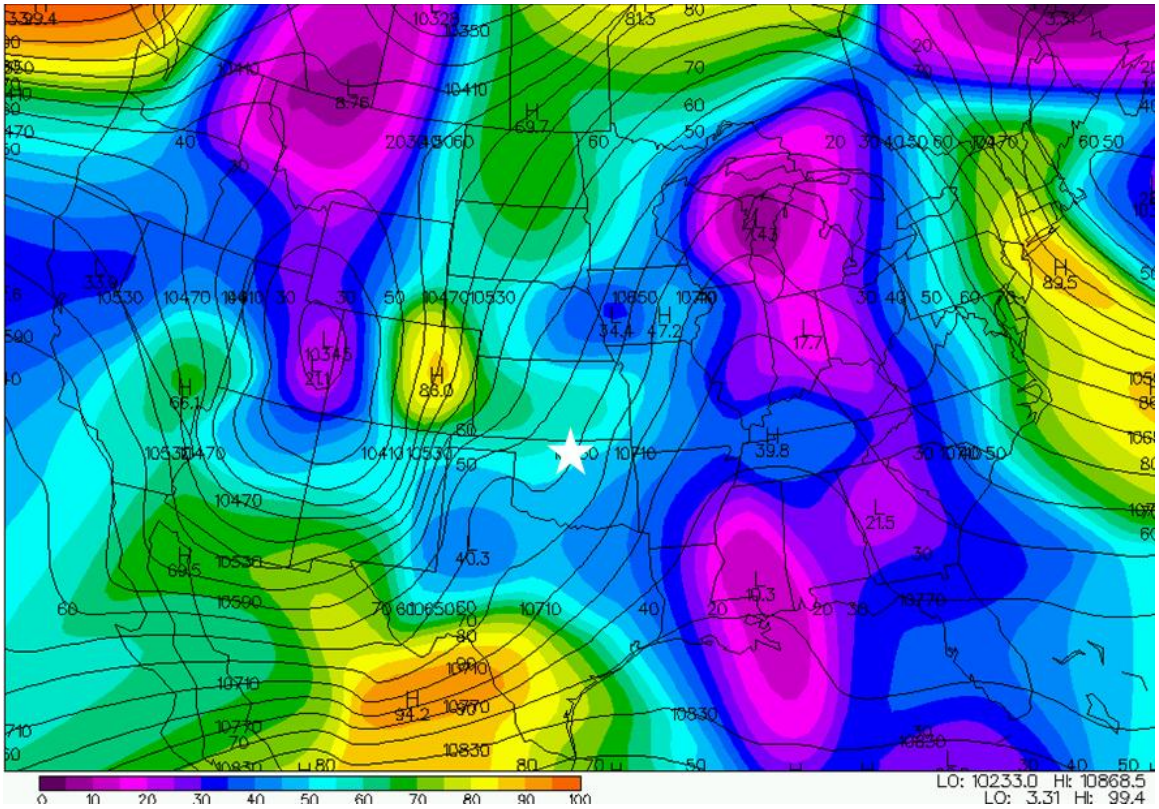

Figure 9: 250 hPa geopotential height in meters (black contours) and isotachs in knots (colored contours) at 12 UTC on 11 May 2011 over the continuous United States. The star denotes location of ARM Central Facility in this and subsequent figures. Image courtesy of the Plymouth State Weather Center.

Figure 10 shows at the surface there was an active weather pattern across much of the United States. At 12 UTC, there were several low pressure systems over the contiguous United States and southern Canada connected by a series of occluded and cold fronts. A cold front extended from a low pressure system in southeastern Minnesota to the southwest into an area of low pressure located over the borders of Colorado, Kansas, Oklahoma, Texas, and New Mexico. South of the low over southeastern Colorado, there was a cold front trailing a dryline, which is marked as a

trough in Fig. 10. Both of these features extended southward from the Oklahoma panhandle and through eastern New Mexico and western Texas. The dryline helped initiate areas of showers and thunderstorms in eastern New Mexico and western Texas, which at 12 UTC were located from southwestern Kansas into western Oklahoma and Texas. The showers located in southwestern Kansas and the Oklahoma and Texas panhandles were also located under the area of divergence at 250 hPa.

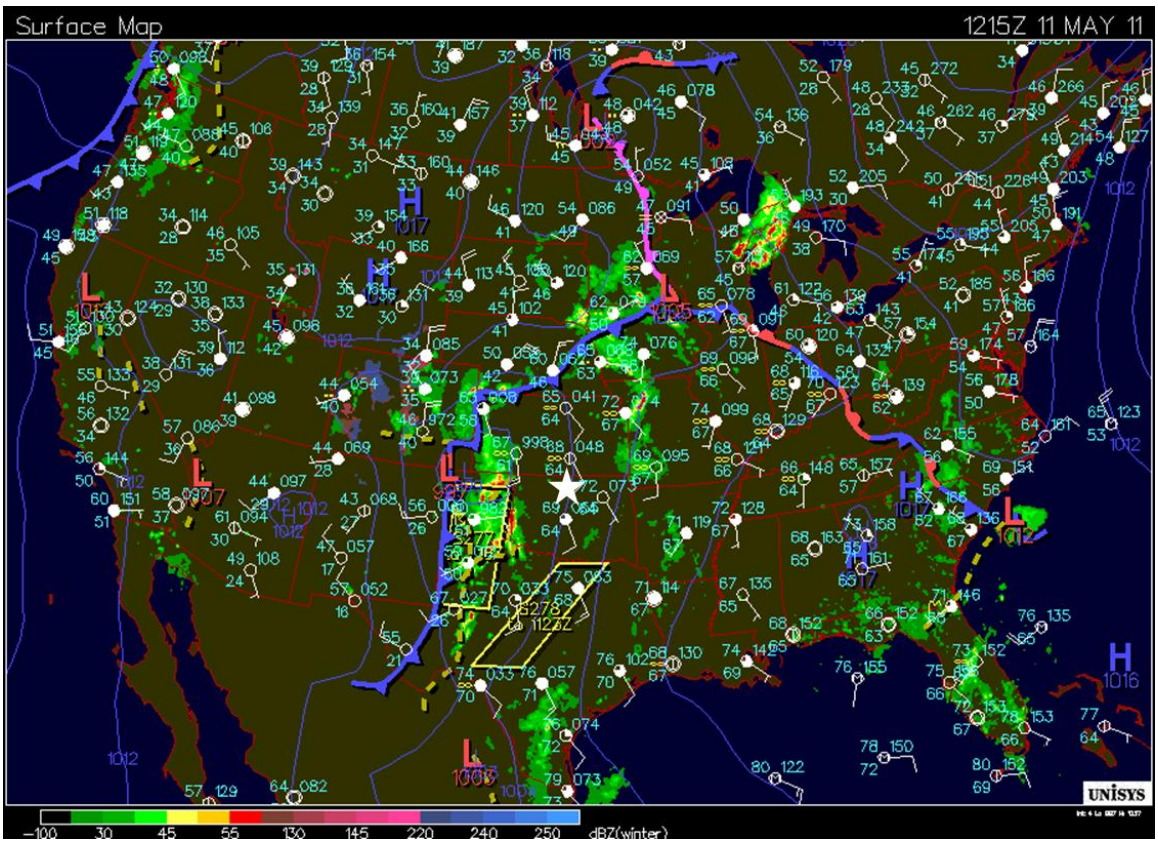

Figure 10: Surface observations, objectively analyzed surface pressure contours (blue), objectively analyzed frontal positions, national base radar reflectively mosaic, Storm Prediction Center (SPC) Severe Thunderstorm watch boxes (yellow boxes) for 12 UTC 11 May 2012. Image courtesy of Unisys Weather Image and Map Archive.

There were several shortwaves present at 12 UTC over the southern Great Plains helping to generate convection. Figure 11 shows a shortwave over northwestern Texas at 500 hPa. At 700 hPa (Fig.12), there was a shortwave extending from southeastern

Colorado through Oklahoma and another shortwave extending southward from northern New Mexico and into western Texas. Figure 13 shows at 850 hPa there was a shortwave extending eastward across the entire width of northern Oklahoma and southern Kansas. A second shortwave extending over northern Texas was accompanied by a tight moisture gradient. The shortwaves across northern Texas and Oklahoma aided in the convection that was ongoing at 12 UTC. The shortwaves in western Texas and New Mexico were likely responsible for helping regenerate and sustain convection through the day.

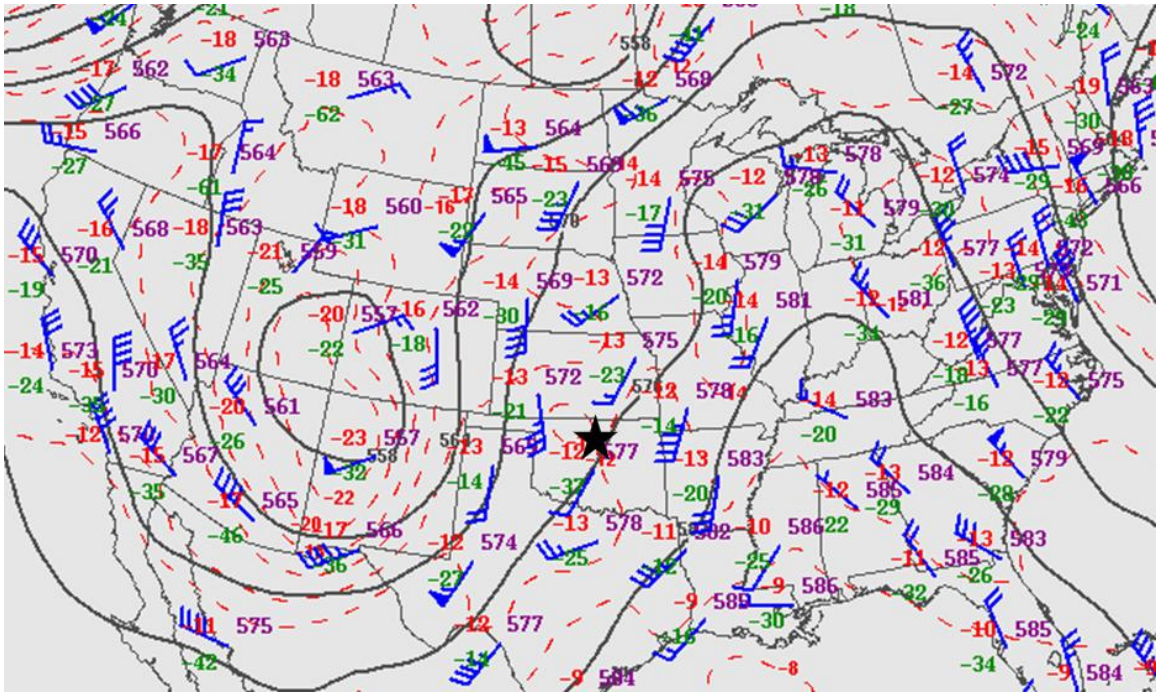

Figure 11: 500 hPa observations, 500 hPa geopotential height (black contours), and 500 hPa temperature (dashed red contours) at 12 UTC on 11 May 2012. Image courtesy of the Storm Prediction Center.

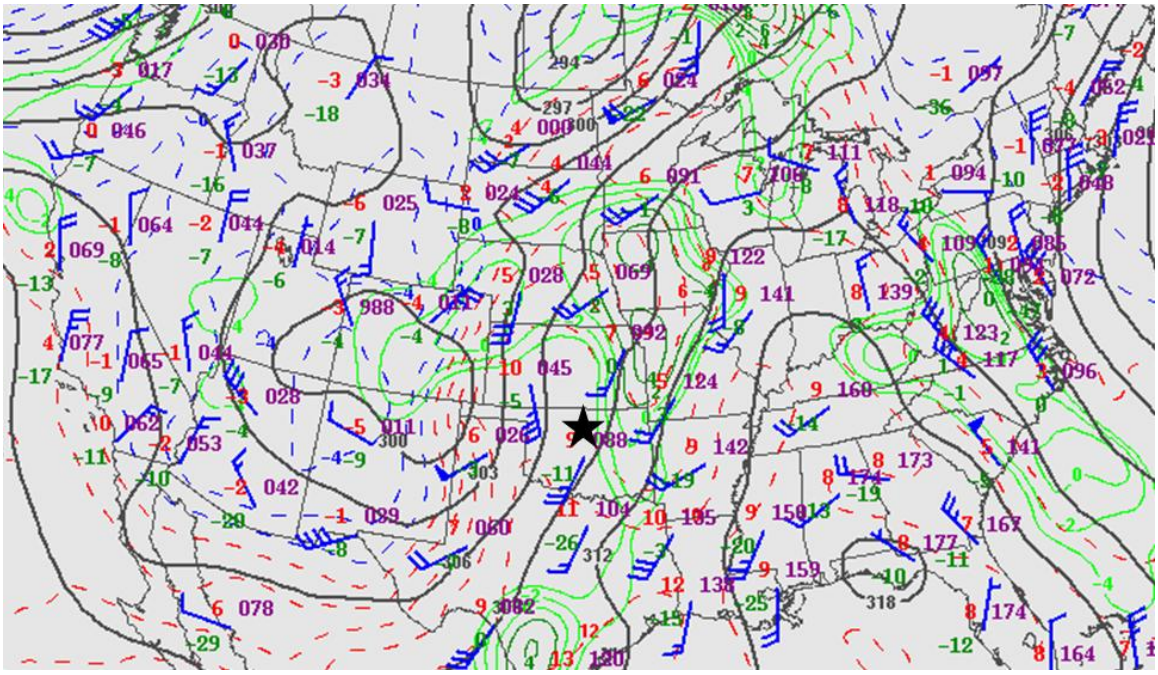

Figure 12: 700 hPa upper air observations, geopotential height (solid black contours), temperature (dashed red contours), and dew point when the dew point is greater than -4 °C (green contours) for 12 UTC 11 May 2011. Image courtesy of the Storm Prediction Center.

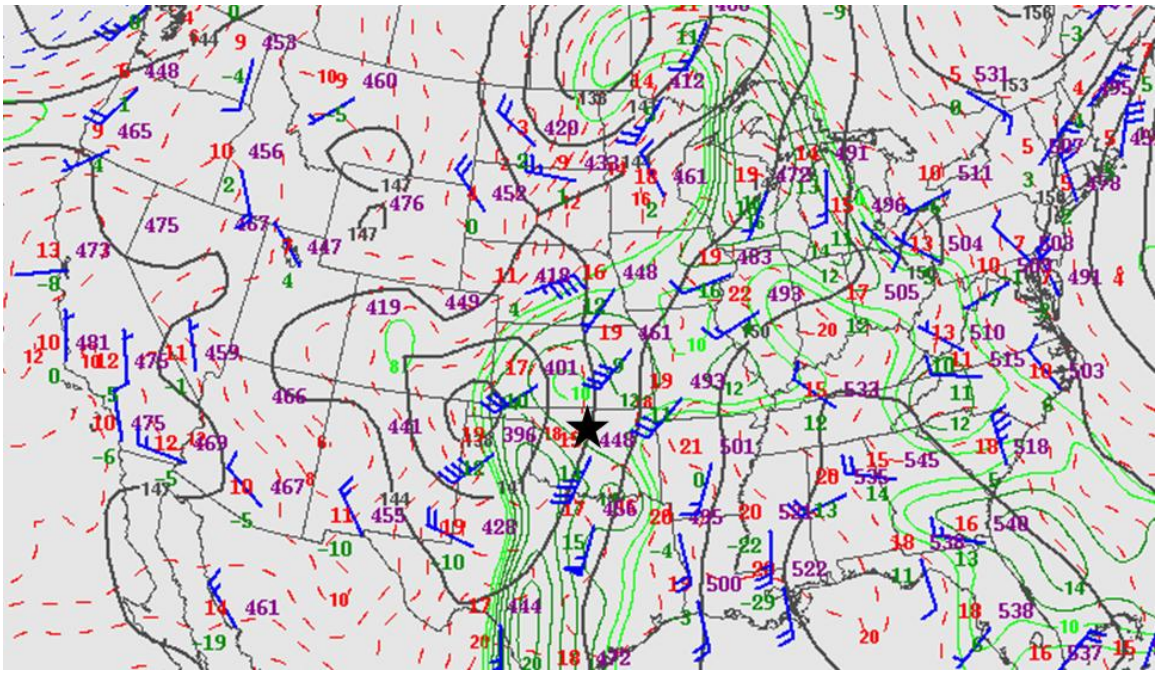

Figure 13: 850 hPa upper air observations, geopotential height (solid black contours), temperature (dashed red contours), and dew point when the dew point is greater than 8 °C (green contours) for 12 UTC 11 May 2012. Image courtesy of the Storm Prediction Center.

Figure 14 shows the evolution of this PS MCS from 12 UTC to 00 UTC on 12 May. At 12 UTC, the MCS was located in the southwestern Kansas and in the Oklahoma and Texas panhandles (Fig. 14a). By 14 UTC, the convective cells were mostly located in either southwestern Kansas or in southwestern Oklahoma, bracketing a large region of mostly stratiform precipitation (Figs. 14b and 14c). At 16 UTC, the stratiform precipitation region had mostly dissipated, but the convection in southwest Oklahoma had begun to strengthen (Fig. 14e). By 17 UTC (Fig. 14f), the MCS had taken on PS MCS characteristics with convection to the right side of the MCS (south) and the stratiform precipitation region to the left (north). The PS MCS retained its shape and characteristics as it traveled northeastward from 17 UTC to 19 UTC (Figs. 14g and 14h). The average storm motion during between 16 and 19 UTC was 22 m s^{-1} towards 21 degrees from north. At 19 UTC, the PS MCS began to merge with convection developing in southern Oklahoma and then with a TS MCS that was over central Texas at 20 UTC (Fig. 14h and 14i) From 20 UTC onwards the combined MCS organized into a TS MCS that continued to propagate eastward through eastern Oklahoma (Figs. 14j through 14l).

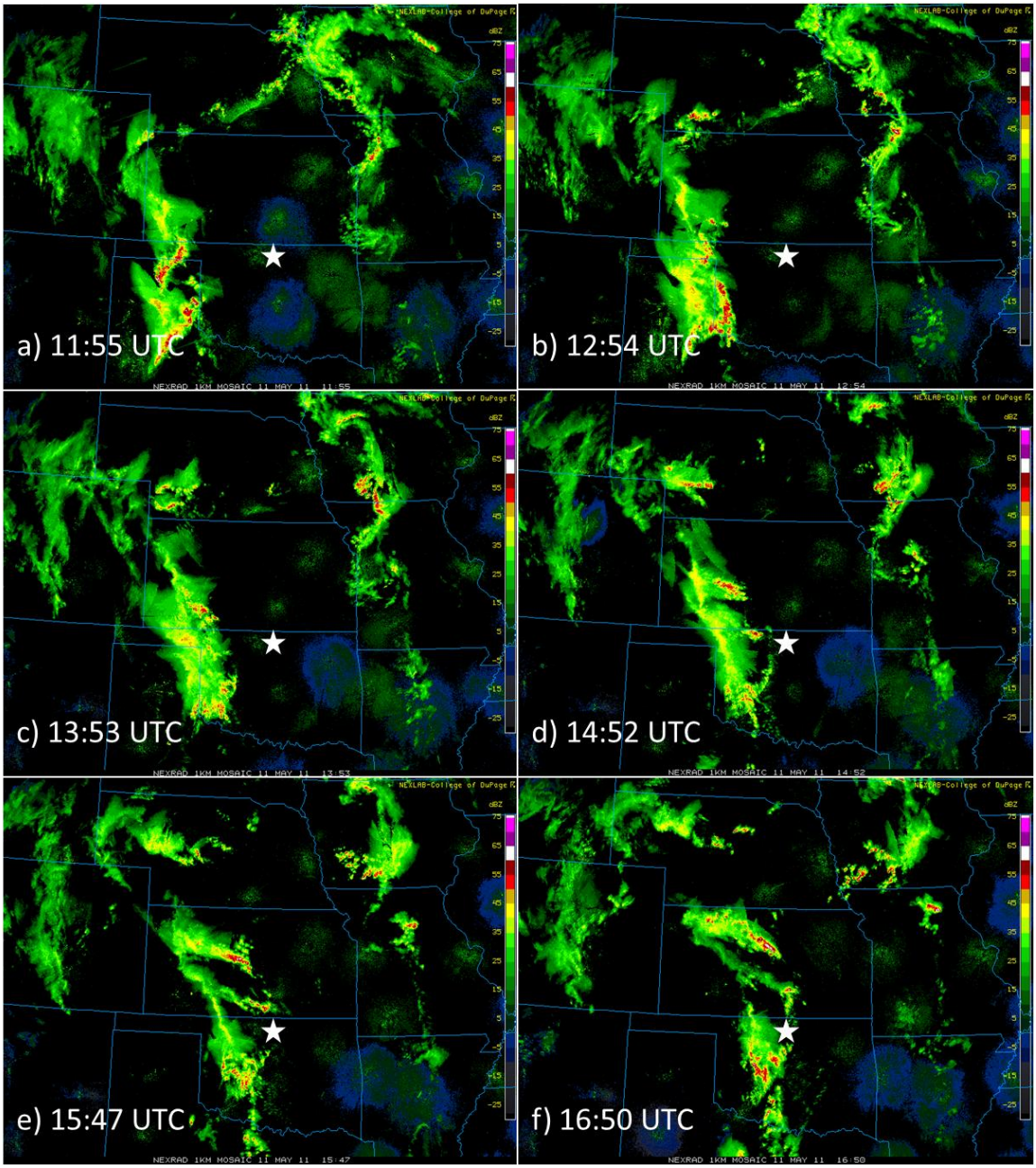

Figure 14: Base radar reflectivity over the central plains for the following times on 11 May 2012: (a) 11:55 UTC, (b) 12:54 UTC, (c) 13:53 UTC, (d) 14:52 UTC, (e) 15:47 UTC, (f) 16:50 UTC, (g) 17:56 UTC, (h) 18:45 UTC, (i) 19:51 UTC, (j) 20:54 UTC, (k) 21:54 UTC, (l) 22:52 UTC.

Figure 14 cont.

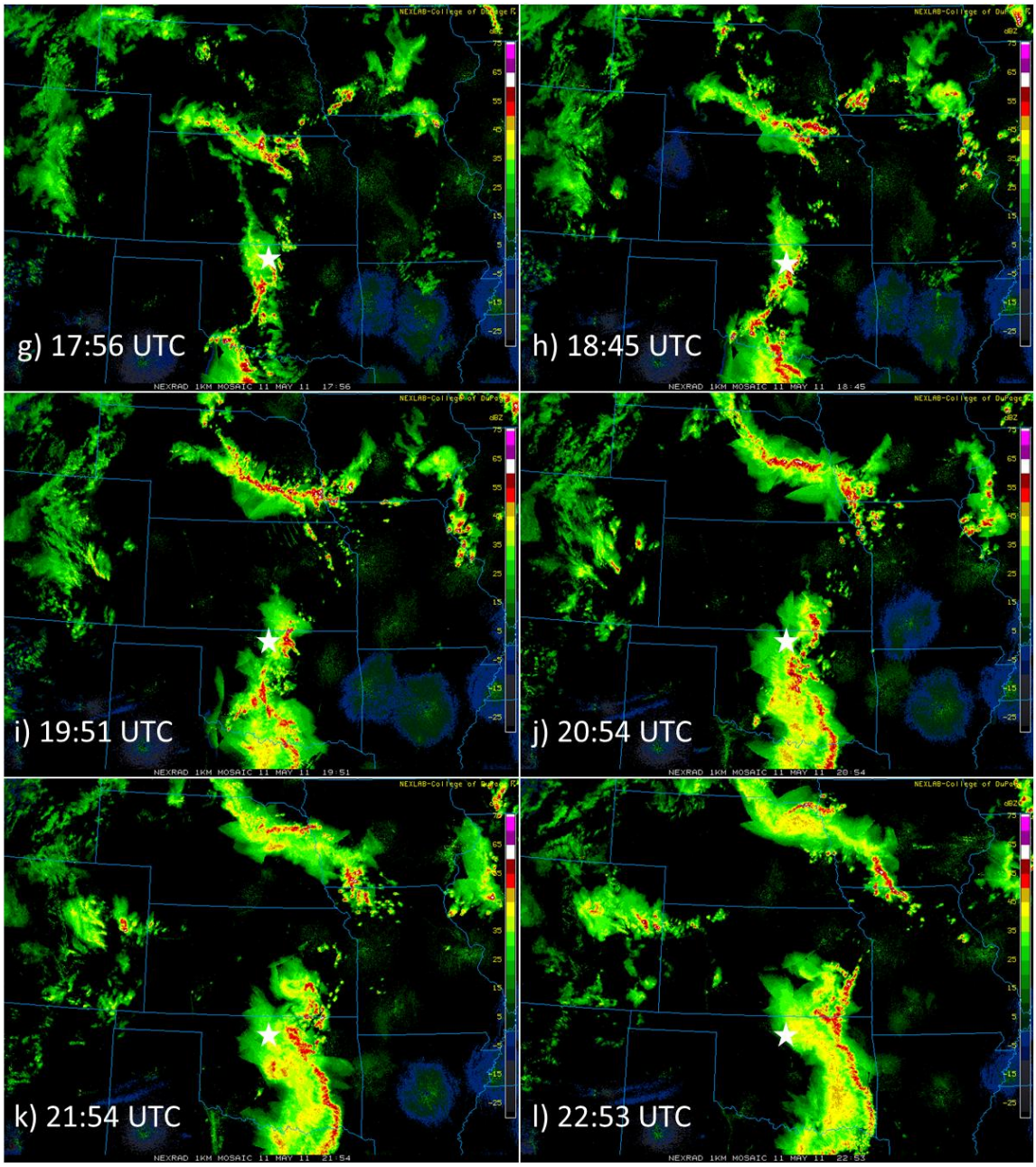

Figure 15a shows that at 12 UTC, divergence was present at 300 hPa over eastern Colorado, western Kansas, Oklahoma, and the Texas panhandle. The divergence over eastern Colorado and western Kansas is due to vertical motions associated with the right entrance region of the jet streak, which is also shown in the 250 hPa observations

(Fig. 9). Figure 15a shows another area of divergence over western Oklahoma and the Texas panhandle in association with the convection that was present at that time. At 15 UTC, the area of divergence moved northeast along with the convection as shown in Fig. 15b. The strongest divergence is present over southwestern Kansas and extreme northwestern Oklahoma and was associated with the northern part of the convection moving through southern Kansas. Figure 15b also shows that the jet stream remained over eastern Colorado and New Mexico, thus not providing any support for the convection occurring in western Oklahoma.

Figure 15c shows that at 18 UTC, diffluence continued to aid in the development of divergence at 300 hPa. The strongest divergence was located over the parallel stratiform region of the MCS. The convective cores of the PS MCS were located in regions of weak divergence at 300 hPa. By 21 UTC, after the PS MCS had turned into a TS MCS, there was a large area of upper-level divergence running from central Kansas to central Texas (Fig. 15d). The strongest divergence continued to be over the stratiform region of the MCS with the convective line ahead of the stratiform region and the most intense divergence.

There was a strong "cap" in place in the atmosphere over southern Kansas and western Oklahoma at 12 UTC. This is shown in Fig. 16 with over 100 J kg^{-1} of Convective Inhibition (CIN) over most of Oklahoma, limiting the amount of new surface-based convection (Fig. 16a). The cap is also clearly shown in Fig. 17 with two temperature inversions below 800 hPa and 537 J kg^{-1} of CIN. Figures 16b and 16c show that the environment in front of the MCS became more conducive to surface-based convection

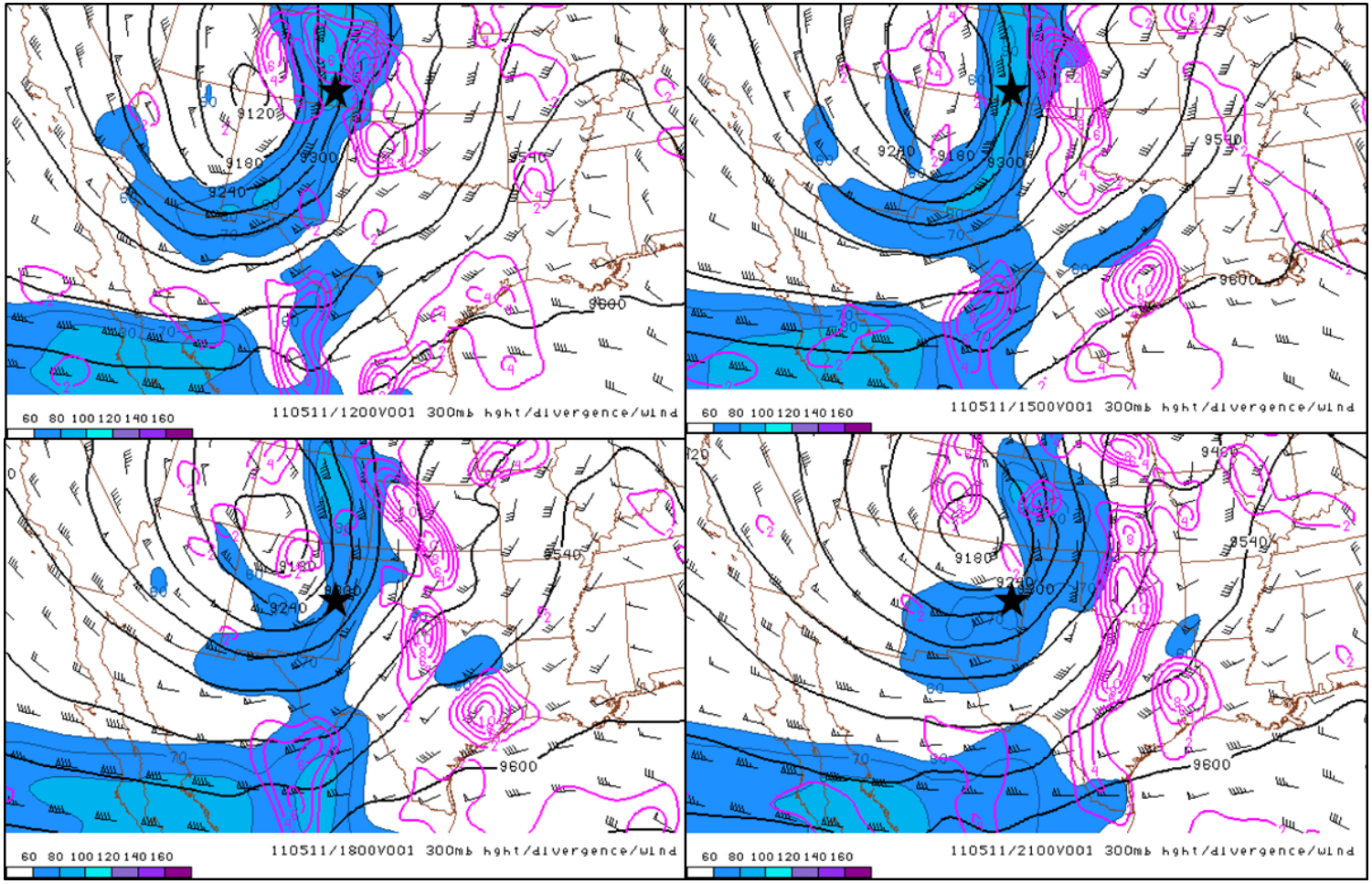

Figure 15: Storm Prediction Center's (SPC) 300 hPa mesoanalysis product with 300 hPa geopotential height in black contours, 300 hPa divergence in magenta contours, and 300 hPa wind for the following times: (a) 12 UTC 11 May, (b) 15 UTC 11 May, (c) 18 UTC 11 May, and (d) 21 UTC 11 May.

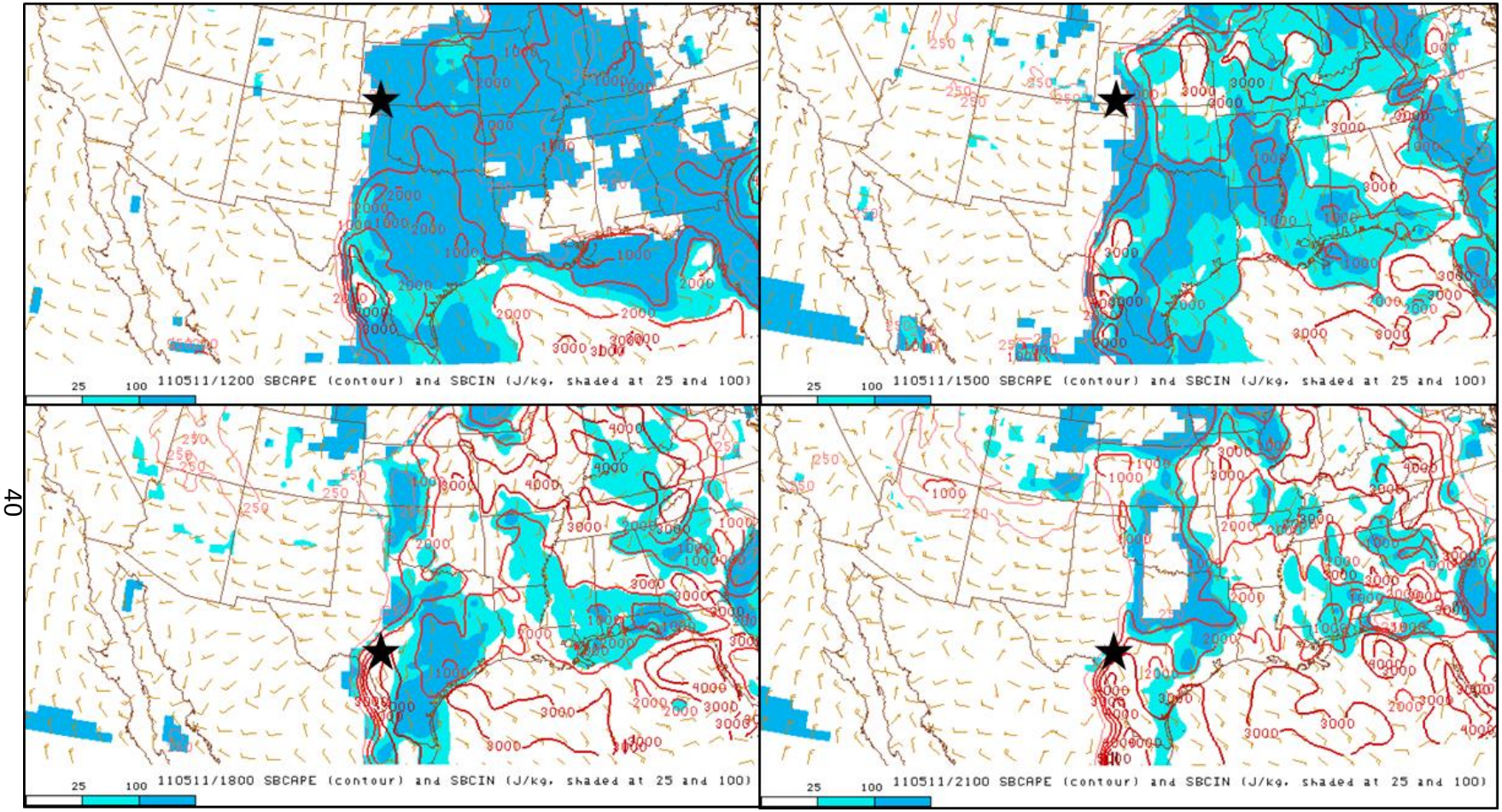

Figure 16: Storm Prediction Center's (SPC) surface-based Convective Available Potential Energy (CAPE) mesoanalysis product showing surface-based CAPE in red contours and surface-based Convective Inhibition (CINH) in filled contours, and surface wind by wind barbs for the following times on 11 May 2011: (a) 12 UTC, (b) 15 UTC, (c) 18 UTC, and (d) 21 UTC.

from 12 to 18 UTC. CIN decreased substantially by 15 UTC (Fig. 16b) and nearly disappeared over Oklahoma by 18 UTC (Fig. 16). The surface-based Convective Available Potential Energy (CAPE) increased to over 2000 J kg^{-1} over most of the eastern half of Oklahoma by 18 UTC. This allowed convection across Oklahoma to redevelop and become more intense.

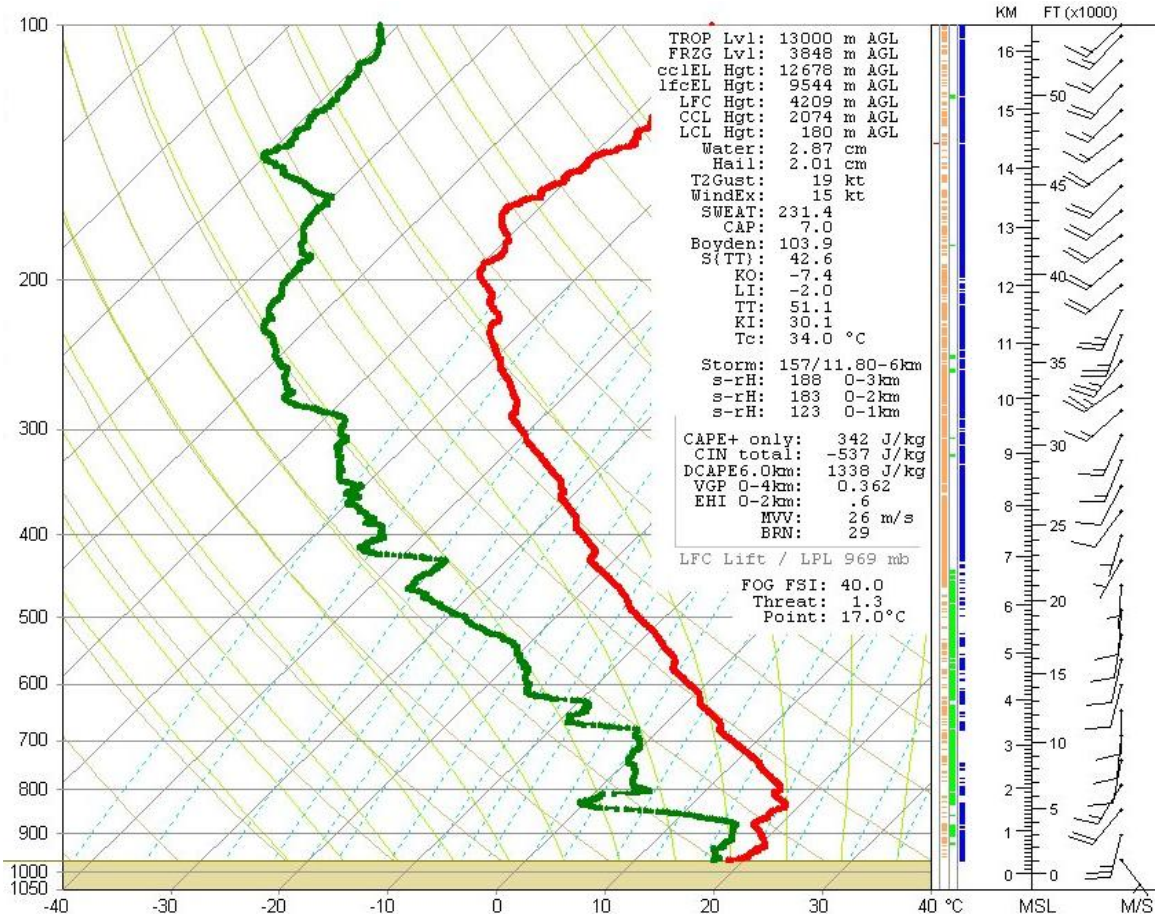

Figure 17: Atmospheric sounding from the ARM Central Facility at 12 UTC on 11 May 2011.

Figure 17 shows the pre-storm thermodynamic profile of the atmosphere over central Oklahoma at 12 UTC. There was a nocturnal temperature inversion present from the surface to near 800 hPa, limiting surface-based convection. However, above

the inversion, there were steep lapse rates (roughly 8.4 °C km^{-1}) from 800 hPa up to 400 hPa. In the presence of a trigger above 800 hPa (which took the form of short wave troughs at 700 hPa and at 500 hPa), these thermodynamic profiles show a suitable atmosphere for elevated convection.

The atmospheric sounding launched at 17 UTC (Fig. 18), which was just prior to when the PS MCS moved over the ARM Central Facility (Fig. 14), represents the pre-storm environment over the ARM Central Facility. At 17 UTC, there were three smaller inversions from the surface to just above 800 hPa. Between and above these inversions, there were near-dry adiabatic lapse rates. This sounding is also more moist than the 12 UTC sounding. Precipitable water from the 17 UTC sounding is 3.48 cm while the precipitable water from 12 UTC is 2.87 cm. Given a small trigger, the 17 UTC sounding is much more conducive to surface-based convection than the 12 UTC soundings.

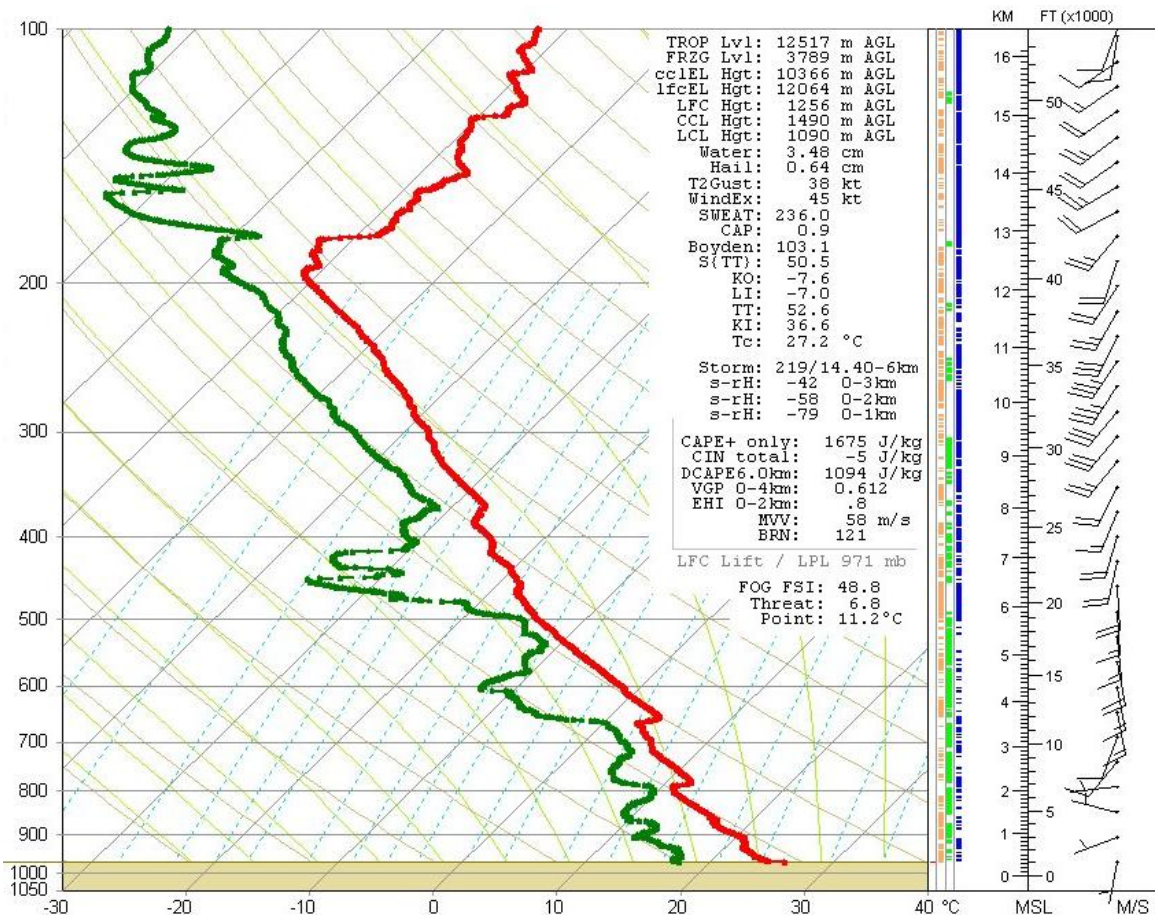

Figure 18: Atmospheric sounding launched from the ARM Central Facility at 17 UTC 11 May 2011.

At 21 UTC, Fig. 16d shows that over central Oklahoma, at the same location as the MCS, there was less than 250 J kg^{-1} of surface-based CAPE and less than 25 J kg^{-1} of surface-based CIN. This is due to the development of a cold pool underneath the MCS. The 00 UTC sounding from Purcell, Oklahoma (Fig. 19) was chosen because it was the closest in time from either Purcell or from ARM Central Facility to represent the 21 UTC environment when a cold pool was present. The temperature profile shows an inversion from the surface to about 925 hPa, which was probably caused by the cold pool. Due to this inversion, there was only 35 J kg^{-1} of CAPE and 409 J kg^{-1} of CIN present.

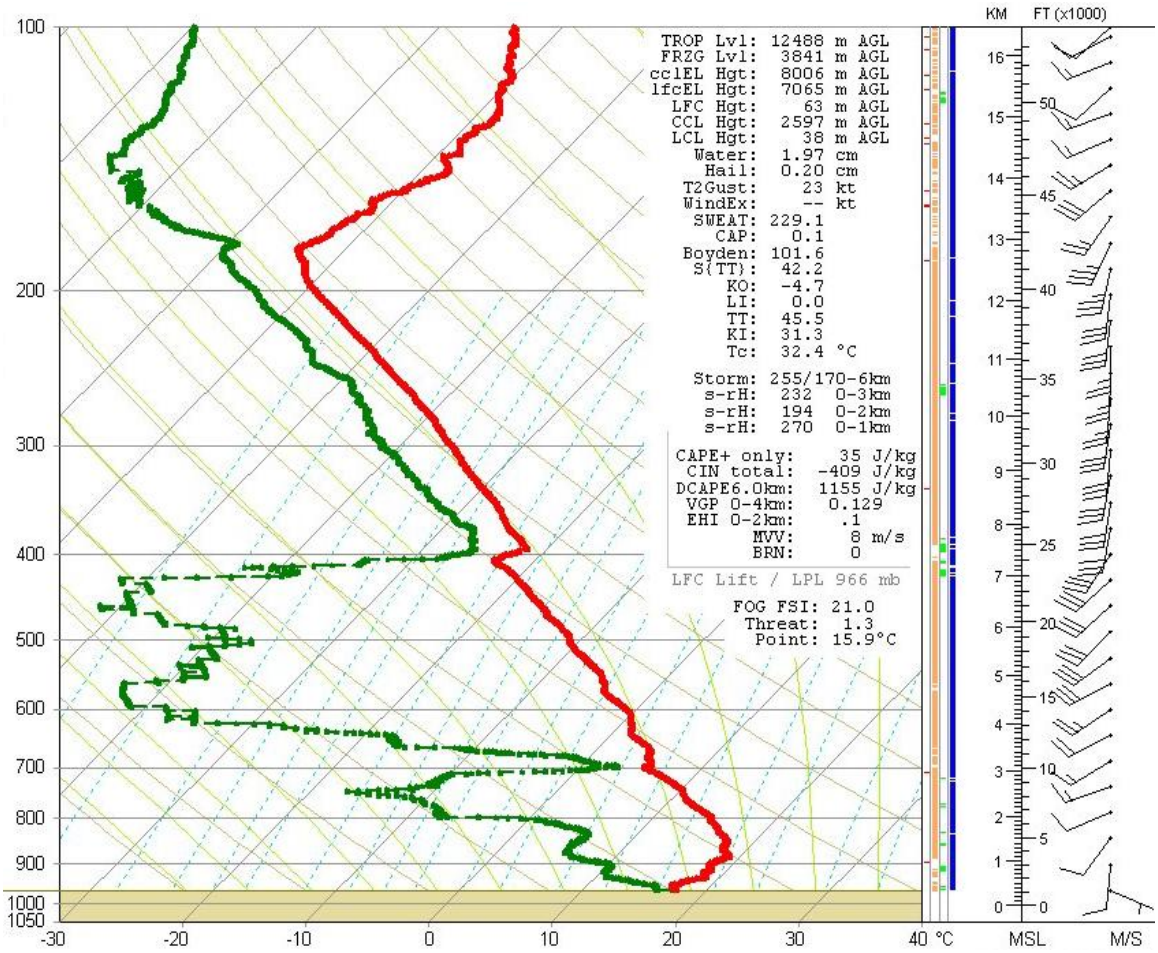

Figure 19: Atmospheric Soundings from Midlatitude Continental Convective Cloud Experiment (MC3E) outer launch site in Purcell, Oklahoma at 00 UTC 12 May 2011.

The cold pool developed between 18 and 21 UTC. Surface temperature beneath the MCS, indicated by the overcast cloud conditions in central Oklahoma, decreased about 5 °F from 18 to 20 UTC. Figure 20e shows a closed 70 °F isotherm over central Oklahoma. An hour later (20 UTC), temperatures to the south and west of this area had also decreased, expanding the area enclosed in the 70 °F isotherm southward into central Texas and westward to just east of the Oklahoma-Texas panhandle border. At this time, the MCS had nearly completed the transition from PS to TS MCS (Fig. 14i). This is a typical pattern of development for PS MCS cold pools. Parker (2007) showed

that cold pools develop near the convective cells, and then expand to the right and rearward in a storm-relative sense. The cold pool also produces rearward accelerations on air parcels that are lifted by the cold pool (Rotunno et al. 1988; Parker and Johnson 2004b). Thus stronger cold pools cause faster transitions from PS into TS MCS (Parker 2007).

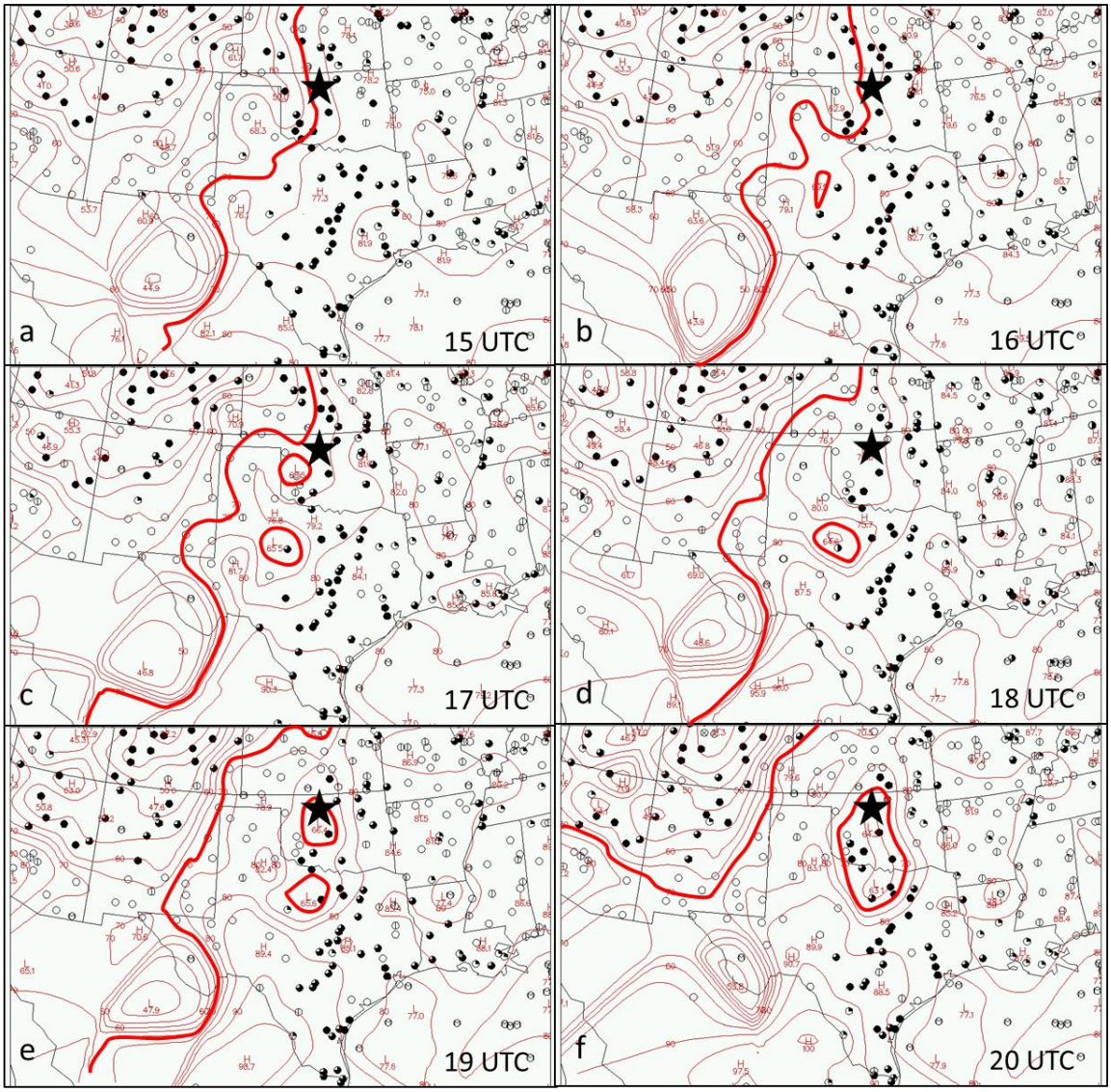

Figure 20: Contoured surface temperature (red) and surface-based cloud cover observations (circles) for each hour from 15 to 20 UTC, inclusive. The 70 °F isotherms are highlighted in thick red line. Images courtesy of Plymouth State Weather Center.

Wind Flow In and Around the MCS

The wind field is provided by rawindsonde, Citation, and Doppler radar observations. Radial velocity data from Doppler radars in the MC3E domain were used to bridge the spatial scale gap between the sounding network and the wind measurements from the Citation and to determine wind flow patterns through the MCS. Horizontal and vertical profiles of the wind velocities were sampled at several different spatial and temporal spacings. The wind velocity fields are presented at the same altitudes as the six Citation level flight legs. The start and stop times for these level legs are given in Table 5.

The vertical wind profile from the 17 UTC sounding launch from the ARM Central Facility has two main features (Fig. 18). The first feature is weak (5 m s^{-1}) veering winds from the surface to 2 km MSL. The wind direction at the surface is from 200 degrees and at 2 km, the winds are nearly westerly. The second feature is stronger winds above 2 km from 160 to 240 degrees with speeds ranging between 10 and 35 m s^{-1}.

Wind measurements obtained with the Citation during the first through the third flight legs (altitudes from 7.5 km to 5.6 km MSL) show a trend of increasing wind speed with decreasing altitude (Fig. 21). The wind at the first level leg was about 25 $\pm$ 5 m s^{-1} and the wind at the third leg was about 30 $\pm$ 5 m s^{-1}. There is also a trend of wind direction becoming more westerly as the Citation descended from 7.5 to 5.6 km. Between the third and the sixth level flight leg (5.6 and 2.8 km), the wind speed decreases with decreasing altitude to 15 $\pm$ 5 m s^{-1}. The wind direction did not show any

height dependence between the third and the sixth flight legs. The wind speed and direction as measured by the Citation also show a dependence on where the measurement was taken relative to the position of the MCS. The first and fifth flight legs traversed from the eastern edge to the western edge of the parallel stratiform region, while the fourth leg crossed from western edge to the eastern edge. Wind measurements from these legs show that wind speed was generally lower on the eastern side of the MCS (beginning of first and fifth legs and end of fourth leg) than on the western edge.

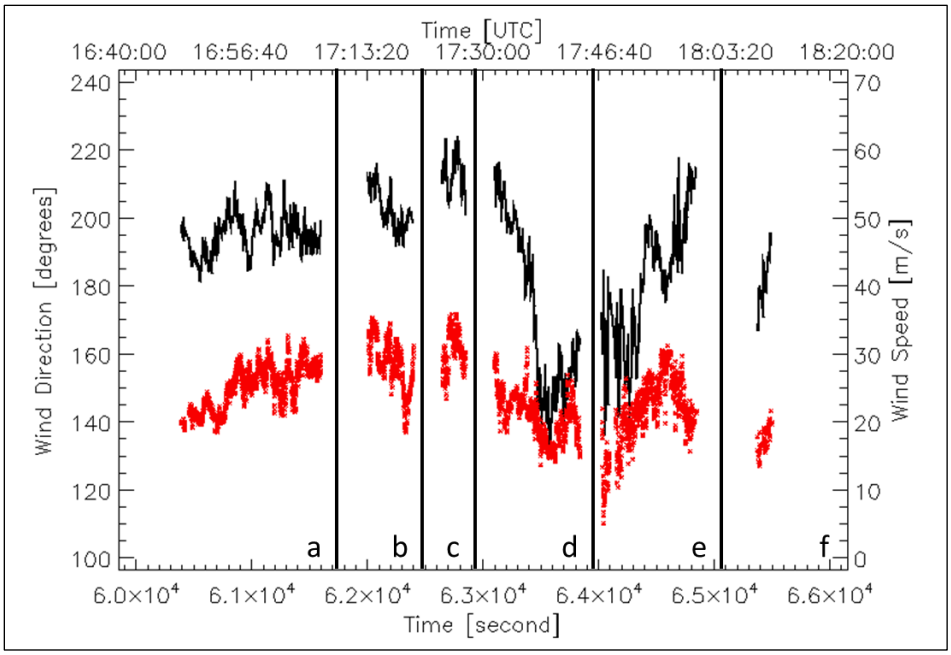

Figure 21: Wind direction (black) and wind speed (red) from the UND Citation on 11 May 2011. There are six level flight legs: (a) east to west flight leg at 7.5 km MSL, (b) west to east flight leg at 6.6 km MSL, (c) east to west flight leg at 5.6 km MSL, (d) west to east flight leg at 4.7 km MSL, (e) east to west flight leg at 3.7 km MSL, and (e) west to east flight leg at 2.8 km MSL.

The wind directions from the 17 UTC SGP sounding are consistent with the Citation measurements on the eastern side of the MCS (Fig. 18). The wind was from the

southwest (about 200 degrees) at 7.4 km and from the southeast (160 degrees) at 3.7 km. The Citation-measured wind in the western part of the MCS at 5.6 km was from the southwest while the sounding indicates southeasterly wind at this level. Wind speeds from the sounding data are between 5 to 10 m s^{-1} slower than wind speeds measured in the western part of the MCS with the Citation.

The orientation of the zero isodop from KVNX and radial velocities from KICT in Figs. 22 through 24 are used to approximate the wind direction and speed at 16:55 UTC. Radial velocities within 40 km of the respective radar are not used due to extrapolation errors. Radar parameters indicate southwesterly winds (210 degrees) with little directional shear over this layer. Maximum wind speeds were greater than 30 m s^{-1} at 3.7, 5.6, and 7.4 km MSL. At 18:09 UTC, Figs. 25 through 27 indicate that the wind within the western half of the MCS was from the southwest from 3.7 km to 7.4 km, while in the eastern half, the wind was from the south. The radar data at 18:09 show that there was little change in wind direction during the time of the Citation flight legs in the western half of the MCS. The radar data at 18:09 UTC show the southerly flow in the eastern part of MCS that the Citation measurements indicate.

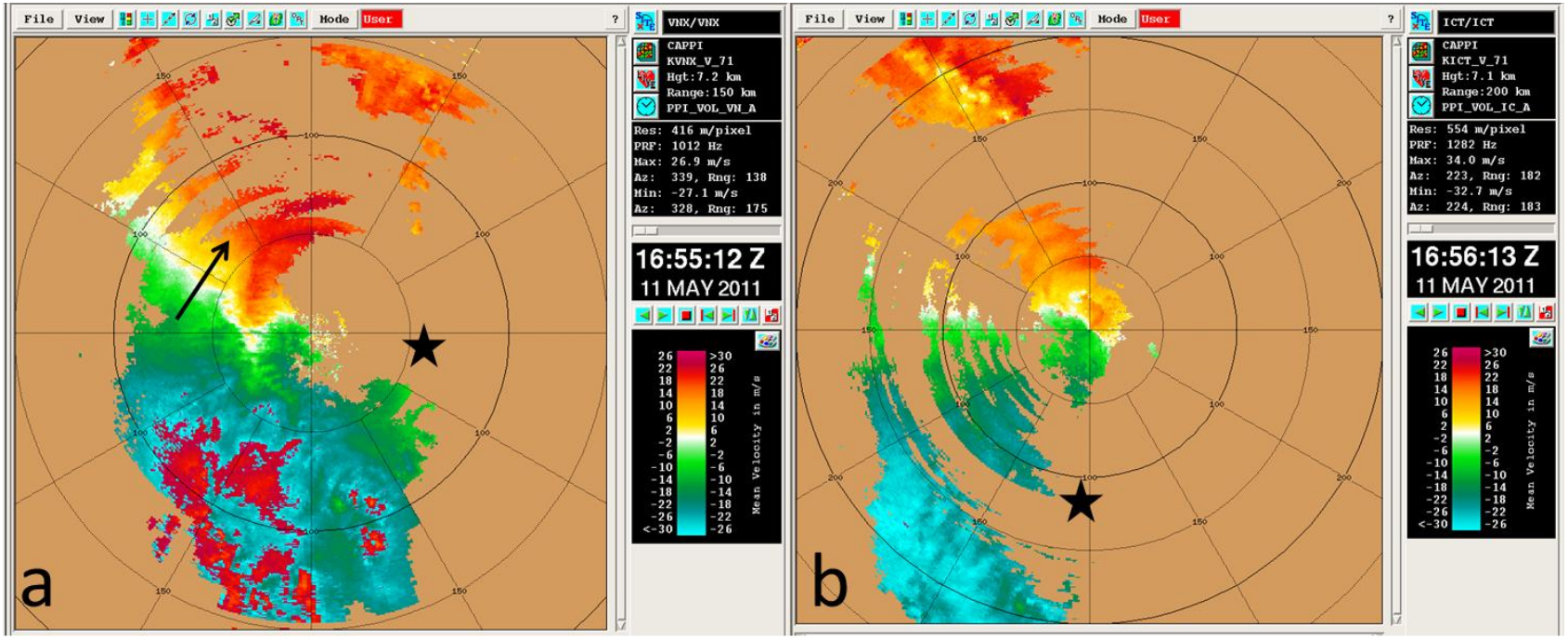

Figure 22: Radial velocity CAPPIs at 7.4 km MSL from (a) Vance Air Force Base, Oklahoma (KVNX) radar on 11 May 2011 at 16:55 UTC and (b) Wichita, Kansas (KICT) radar at 16:56 UTC. Arrow indicates wind direction across the zero isodop.

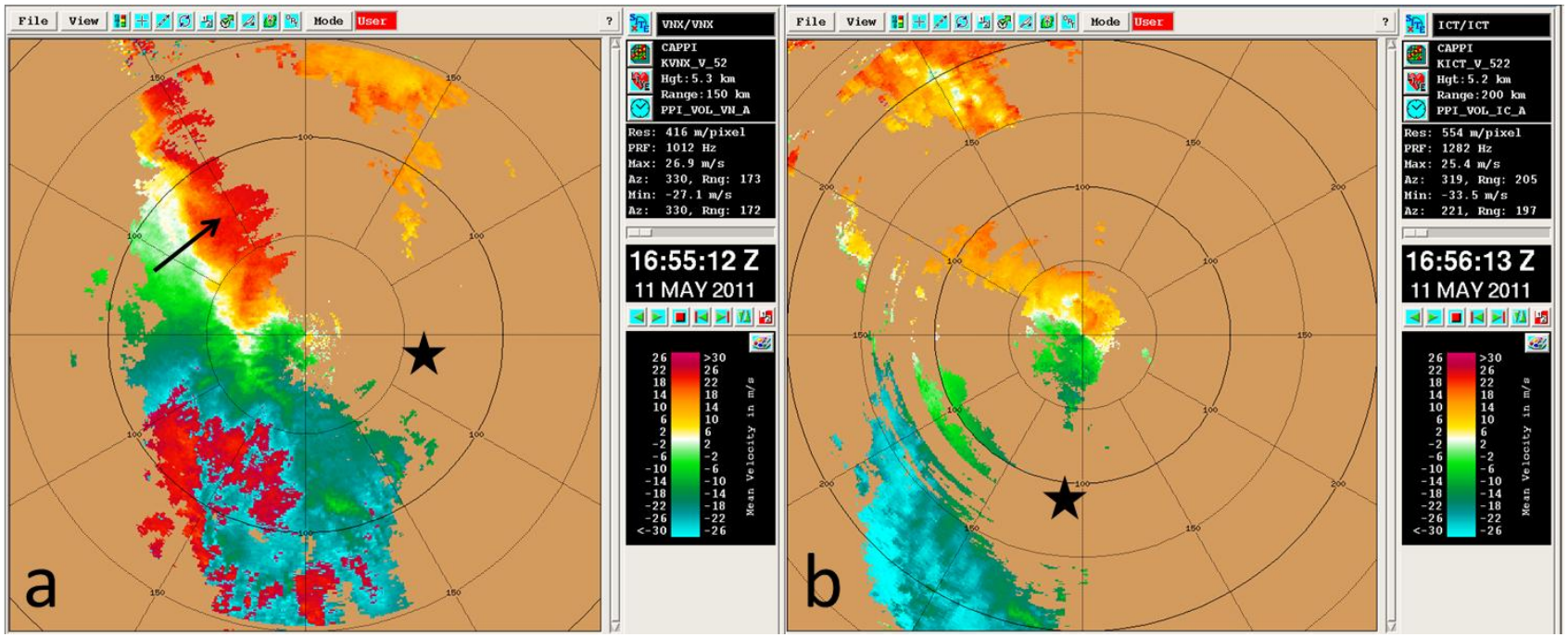

Figure 23: Radial velocity CAPPIs at 5.6 km MSL from (a) Vance Air Force Base, Oklahoma (KVNX) radar on 11 May 2011 at 16:55 UTC and (b) Wichita, Kansas (KICT) radar at 16:56 UTC. Arrow indicates wind direction across the zero isodop.

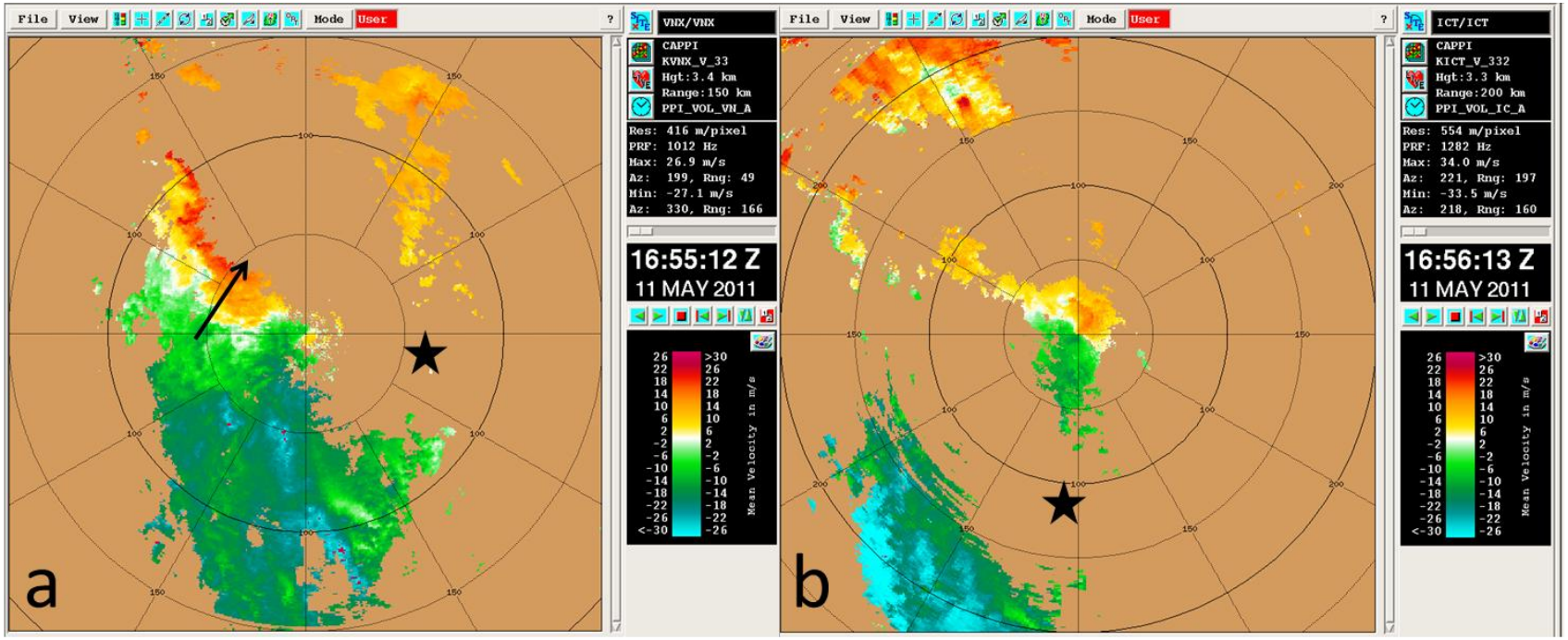

Figure 24: Radial velocity CAPPIs at 3.7 km MSL from (a) Vance Air Force Base, Oklahoma (KVNX) radar on 11 May 2011 at 16:55 UTC and (b) Wichita, Kansas (KICT) radar at 16:56 UTC. Arrow indicates wind direction across the zero isodop.

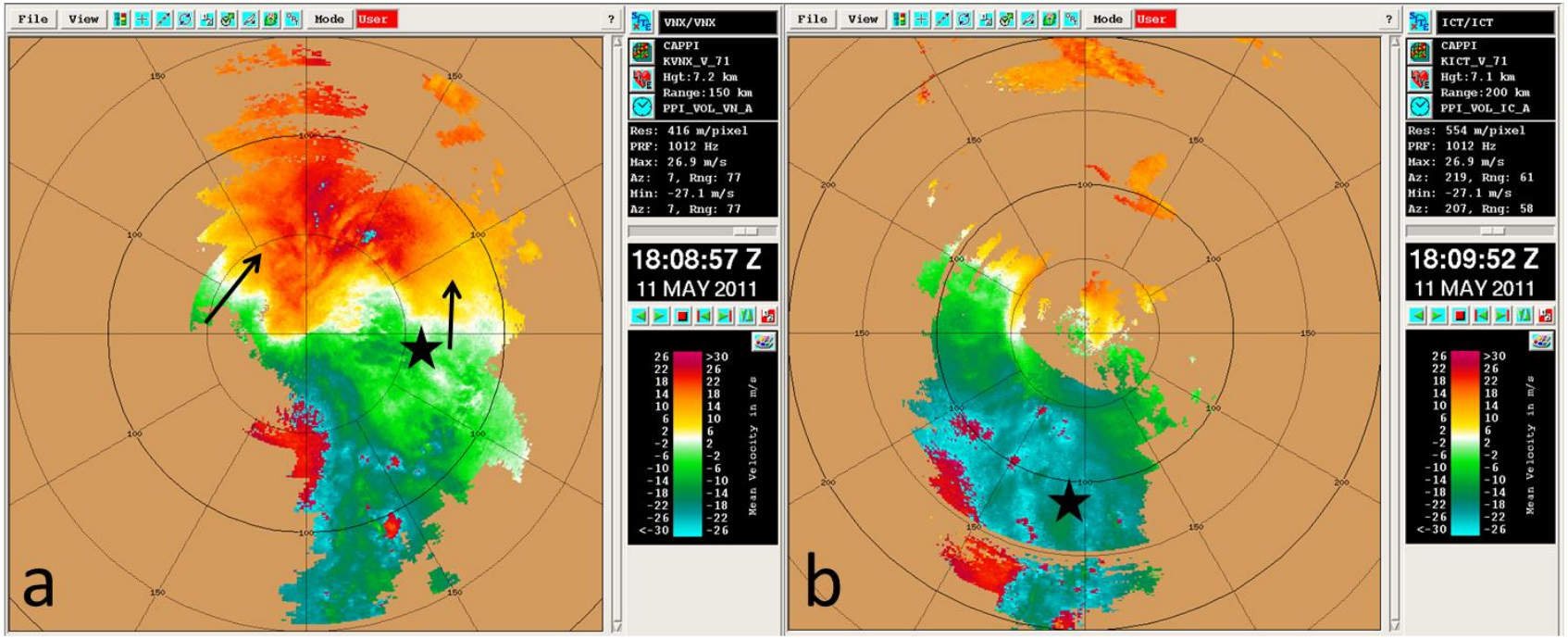

Figure 25: Radial velocity CAPPIs at 7.4 km MSL from (a) Vance Air Force Base, Oklahoma (KVNX) radar on 11 May 2011 at 18:09 UTC and (b) Wichita, Kansas (KICT) radar at 18:10 UTC. Arrows indicate wind direction across the zero isodop.

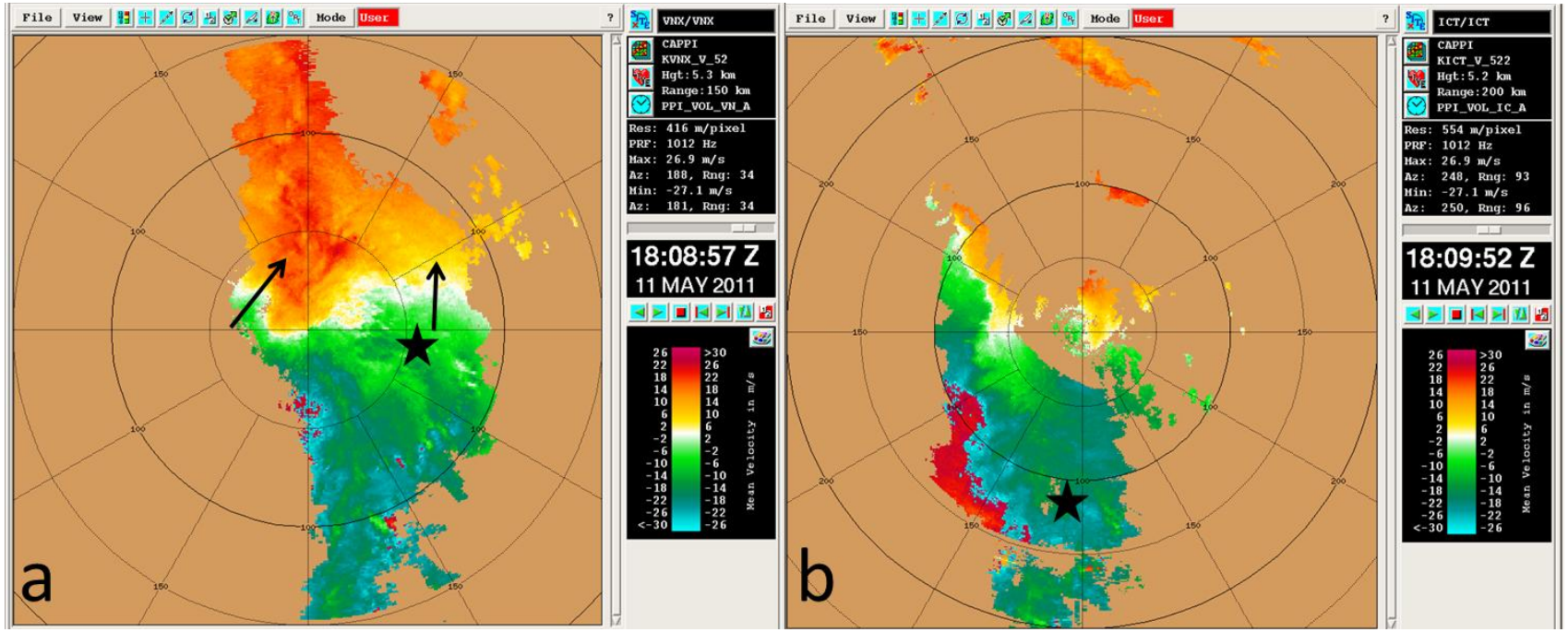

Figure 26: Radial velocity CAPPIs at 5.6 km MSL from (a) Vance Air Force Base, Oklahoma (KVNX) radar on 11 May 2011 at 18:09 UTC and (b) Wichita, Kansas (KICT) radar at 18:10 UTC. Arrows indicate wind direction across the zero isodop.

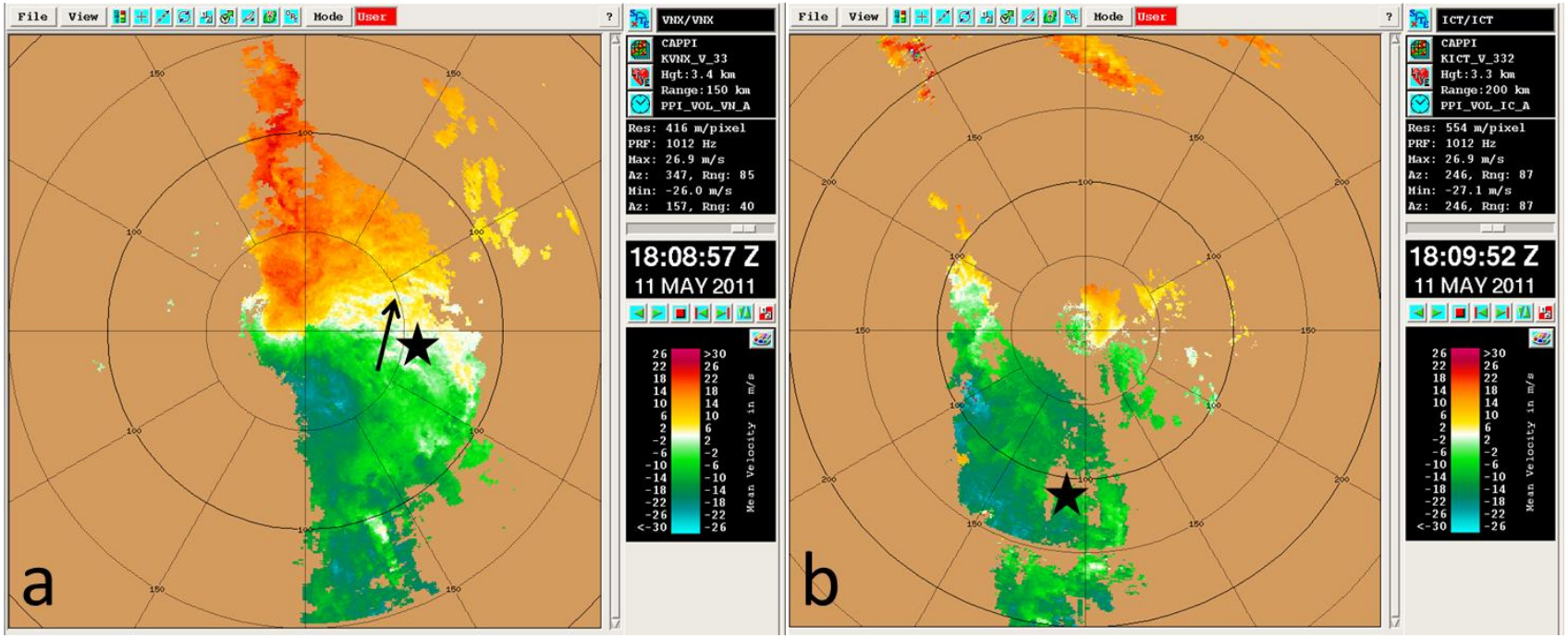

Figure 27: Radial velocity CAPPIs at 3.7 km MSL from (a) Vance Air Force Base, Oklahoma (KVNX) radar on 11 May 2011 at 18:09 UTC and (b) Wichita, Kansas (KICT) radar at 18:10 UTC. Arrow indicates wind direction across the zero isodop.

Based on the east-west wind component from the NPOL radar (Fig. 28), the MCS can be divided into six parts: the front (eastern) lower, middle, and upper portions; and the rear (western) lower, middle, and upper portions of the storm. The front lower portion was generally characterized by weak westerly ground-relative flow while the rear lower portion was characterized by weak ground-relative easterly flow. The front middle portion had stronger (between 5 and 10 m s^{-1}) ground-relative easterly flow while the rear middle portion had strong ground-relative westerly flow (between 10 and 20 m s^{-1}). There was typically a horizontal gap of about 50 km between the strongest areas of easterly and westerly flow. The front upper portion was characterized by areas of stronger ground-relative westerly flow (10 to 15 m s^{-1}), but usually not as strong as the rear middle portion. The rear upper portion was characterized by weak ground-relative easterly flow (less than 5 m s^{-1}).

The wind speeds measured with the radars are consistent with the speeds measured with the Citation through the whole profile. However, the Citation measured a shift in wind direction from 210 degrees to 150 degrees at altitudes of 4.7 and 3.7 km that is not apparent in the radar data. Wind measurements from NPOL are consistent with the measurements obtained with the Citation data. Measurements obtained with NPOL show weak westerly flow across the MCS at an altitude of 7.5 km, which when combined with KVNX radial velocities indicating southerly flow, indicate south-southwesterly flow. The Citation data shows the wind was from the south-southwest (195 $\pm$ 10 degrees), which agrees with the radar data. At 3.7 km, measurements

obtained with NPOL show easterly wind in the eastern part of the stratiform region and westerly wind in the west, which corresponds well with the wind shift seen during the fifth Citation flight leg.

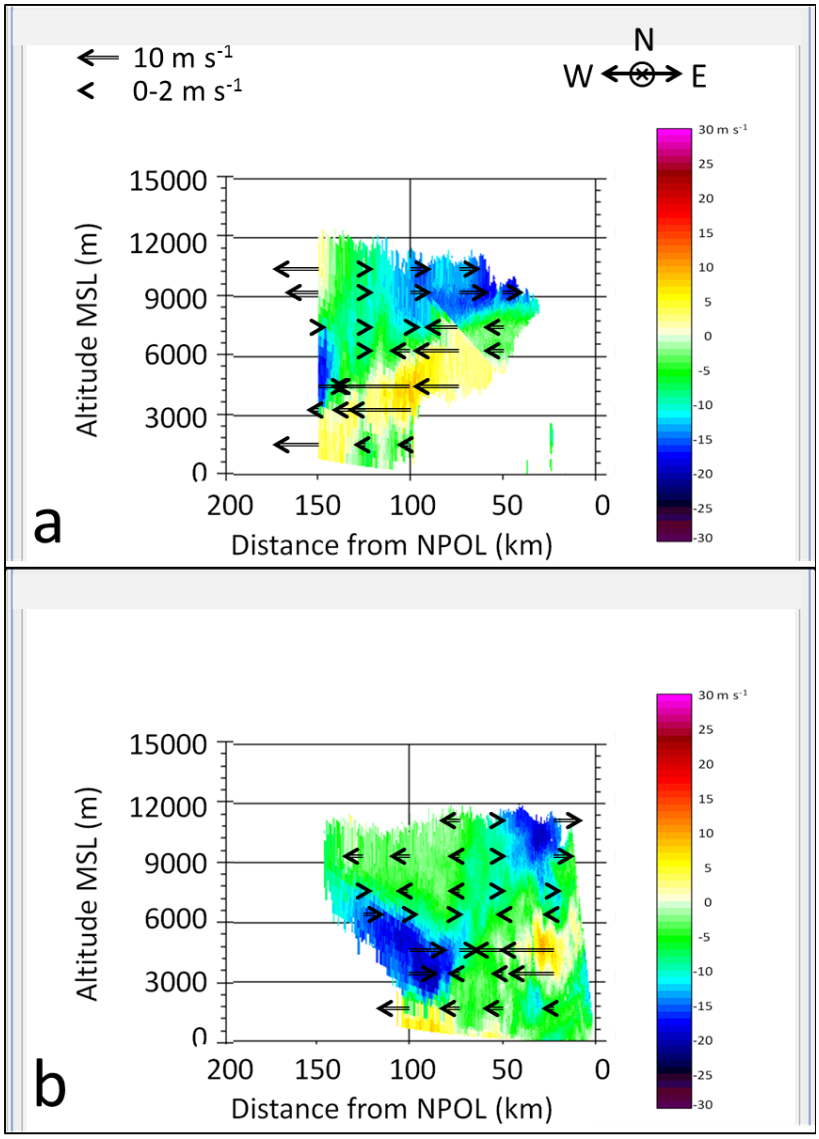

Figure 28: NASA S-Band Transportable Dual Polarimetric Radar (NPOL) Relative Height Indicator (RHI) scans showing ground-relative radial velocity (in color, m s^{-1}) and storm-relative radial velocity (arrows, m s^{-1}) along the 270° radial (due west) for the following times on 11 May 2011: (a) 16:55, (b) 18:08 UTC. Plot orientation is such that east is to the right and north is into the figure. Vector with tail denotes wind speed of 10 m s^{-1} while vector with no tail denotes wind speed between 0 and 2 m s^{-1}.

Observed winds from soundings, radar, and the Citation show that winds in the 3.7 to 7.5 km layer were dominated by a southerly component (140 to 220 degrees). Parker (2007) found that most of the northward hydrometeor flux in their simulated PS MCS occurred in the middle- to upper troposphere [5 – 12 km above ground level (AGL)]. Soundings show that the ground-relative wind in the 8.5 to 11.5 km layer was from about 210 degrees between 25 and 35 m s^{-1}. The corresponding storm-relative winds in this layer were from 203 to 256 degrees between 5 and 24 m s^{-1}. Thus, the storm-relative wind direction was such that hydrometeors would have been advected northward, which is consistent with the findings of previous studies. This also shows that the vertical wind structure over Oklahoma was responsible for the PS characteristics of the MCS. .

Parker (2007) ran several simulations of a PS MCS. Figure 29 shows an easterly storm-relative flow into the front half of the storm between 10 and 20 m s^{-1} from 1.5 to 6 km in the vertical. About halfway through the highest reflectivity core, the easterly wind flow splits into two streams: one descending to the 1 to 2 km AGL region in the rear of the storm, and the second ascending to the 7 to 12 km region in the rear of the storm. Some of the ascending easterly flow is overturned and becomes westerly flow in the 9 to 12 km region in the front of the storm. In the simulated storm, there is weak flow between these three features.

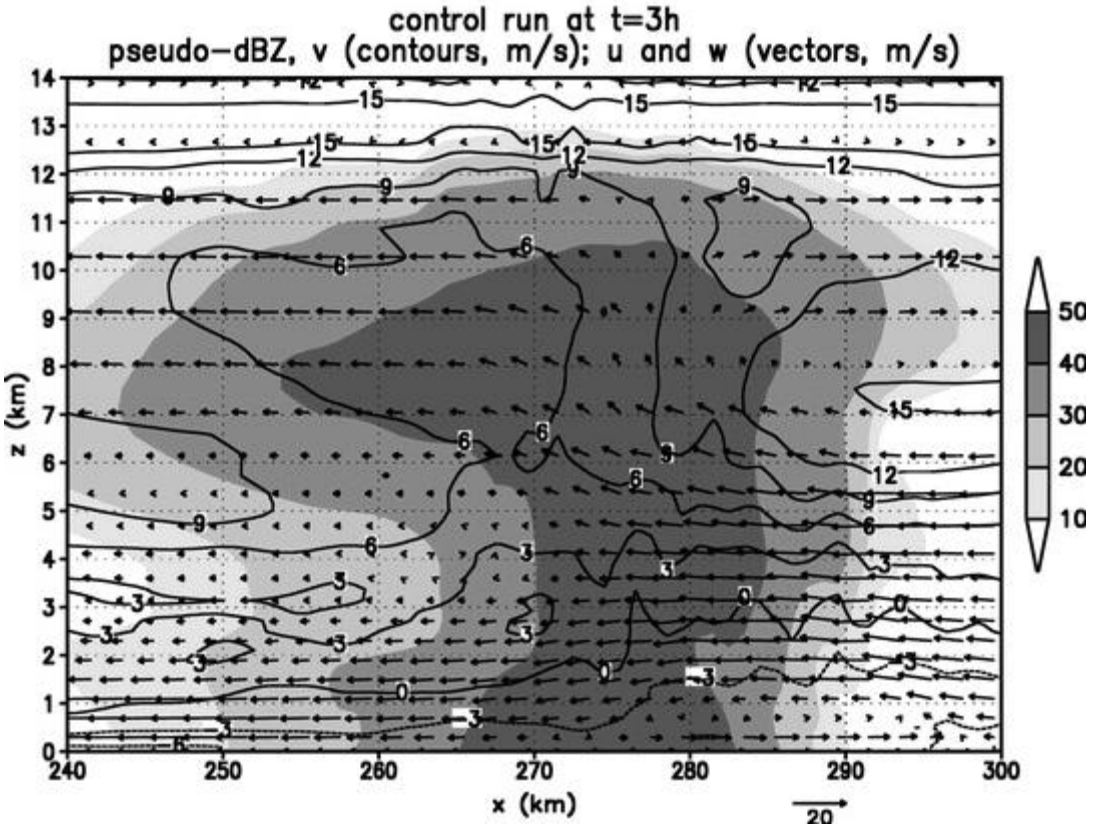

Figure 29: Output for control PS MCS simulation from Parker (2007) at t = 3 h. Vertical cross section of along-line averaged (from y = 250-350 km) radar reflectivity (simulated), shaded, line-parallel wind (*v,* contoured, m s^{-1}), and line-perpendicular circulation (*u* and *w* vectors, m s^{-1}). Reflectivity is only shaded for values of hydrometeor mixing ratio ≥ 1 × 10^{-3} g kg^{-1}. This figure is reproduced from Parker (2007).

NPOL measurements of the u-component of the storm-relative wind in the 11 May 2011 storm show a similar wind flow pattern through the MCS (Fig. 28). The only exception is that the upper-level easterly storm-relative flow is much weaker than the outflow in the simulated MCS at 18:09 UTC (Fig. 28b). A major difference between the actual and the simulated storms is a region of storm-relative westerly inflow between 5 and 10 m s^{-1} in the rear of the observed MCS that is not present at all in the simulated storm. In the same region, the simulated storm has easterly wind at speeds less than 5

m s^{-1}. If this is a rear inflow jet, it may explain the weak westerly storm-relative wind velocities extending from the rear inflow region to the upper outflow region in the front of the storm.

At the surface, the simulation produced northerly wind velocities over 3 m s^{-1}. The line-parallel wind became zero between 1 km (in the rear of the storm) and 3 km (in the front of the MCS). Maximum line-parallel wind speeds behind the storm were 9 m s^{-1} between 5 and 7 km and in front of the storm the line-parallel component was about 15 m s^{-1} between 7 and 8 km. Between these two areas, the line-parallel wind through the center of the MCS was between 6 and 12 m s^{-1}. Line parallel storm relative winds are estimated using measured Doppler velocities along the 0/180 radials and a mean northward storm-motion component of 21 m s^{-1}. At 5.6 and 7.4 km, the largest observed storm-relative line-parallel wind speeds are about 9 m s^{-1}. At the 5-7 km height in the simulated storm, the line parallel wind was between 3 and 15 m s^{-1} to the north, with the 15 m s^{-1} occurring just to the front of the MCS. At 3.7 km in the observed storm, the storm-relative wind was about 4 m s^{-1}. This is slightly stronger than the simulated storm at this level, which had northerly line-parallel wind speeds between 0 and 3 m s^{-1}.

Parallel Stratiform Region Microphysics

Figures 30 and 31 show the environmental characteristics of the parallel stratiform region as derived from the Citation data collected during the six level flight

segments (Table 4). The stratiform region was saturated with respect to liquid water and supersaturated with respect to ice during the first level flight leg (at 7.5 km). Except for the first 100 seconds of the first leg in which the Citation was near the edge of the parallel stratiform region, the relative humidity with respect to ice at this altitude was between 110 and 150 %. High supersaturations such as this have been found in cirrus (Ström et al. 1997; Garrett et al. 2004; Gayet et al. 2004; Jensen et al. 2005) and in thunderstorm anvils near convective cores (Heymsfield et al. 2005).

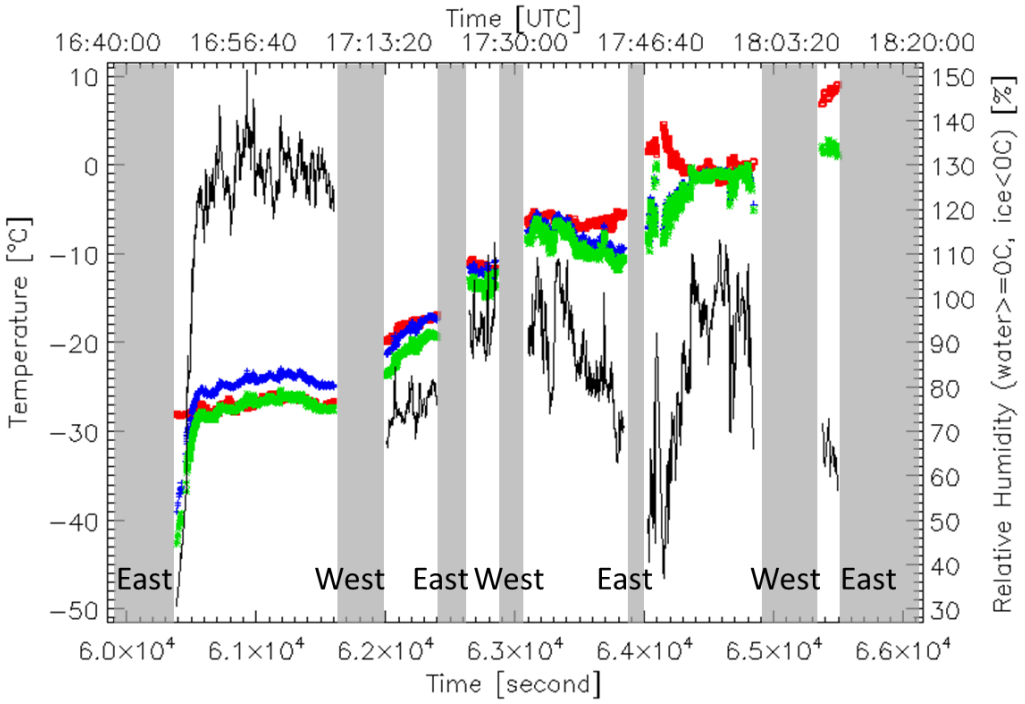

Figure 30: Temperature (red), dew point (green), and frost point (blue) in degrees Celsius; and relative humidity (black) with respect to ice when $T < 0$ and with respect to liquid water when $T \geq 0$ °C from the UND Citation during the six level legs when the Nevzorov total water content was greater than 0.01 g m^{-3} on 11 May 2011. Frost point was set equal to the dew point at temperatures greater than 0 °C. Shaded portions are during ascents, descents, and course reversals. 'East' and 'West' mark the position of the Citation at the beginning and end points of each leg. For example, the second flight leg starting at 17:13:30 traversed from west to east.

Horizontal variability in the relative humidity field was present in the stratiform region. As stated previously, the fourth level flight leg extended from the western edge of the parallel stratiform region to the eastern edge, while the fifth flight leg extended from the eastern extent to the western extent of the region. Both flight legs show a trend of increasing relative humidity with increasing distance from the eastern edge of the stratiform region, which is likely due to entrainment. Figures 26 and 28 show that the wind was southeasterly in the eastern part of the MCS at 4.7 and 3.7 km (the altitudes of the fourth and fifth flight legs), which would support entrainment of non-saturated pre-storm air (Fig. 18).

Figure 31 shows a trend of decreasing TWC with decreasing height (increasing temperature). Assuming that the TWC measured with the Nevzorov probe is approximately equal to the total water mass of the cloud and precipitation, this result is consistent with the results of McFarquhar et al. (2007) for TS MCSs. Very little liquid water was present in the parallel stratiform region as shown by the Cloud Droplet Probe (CDP) liquid water content (LWC) and the Rosemount[2] Icing Detector (RICE) frequency in Fig. 32. Liquid water was present during legs 3 and 4, evident by LWC over 0.05 g m^{-3} and reductions in RICE frequency (Fig. 32). During times of higher LWC, the Citation was near the western edge of the precipitation region, which had some stronger base tilt KVNX radar reflectivities. Figure 33 shows that a small region of higher reflectivity was present within the parallel stratiform region southwest of the Citation at 17:31 UTC,

[2] The former Rosemount Company is now a part of the Goodrich Aerospace Sensors Division.

showing the presence of embedded convection that may be associated with some liquid water.

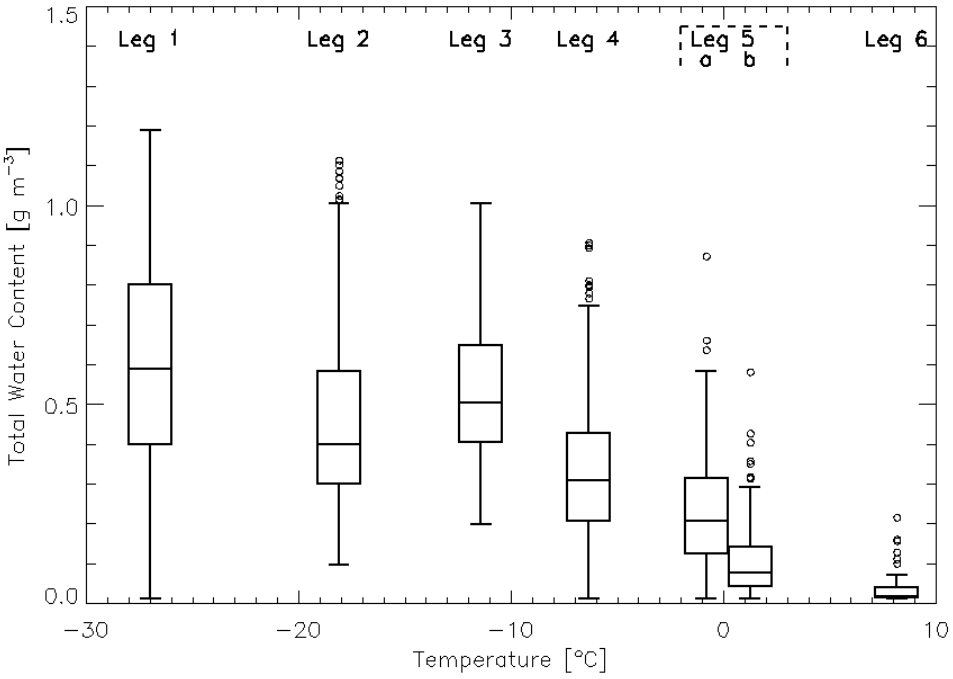

Figure 31: Boxplot showing variation of total water content as a function of temperature between 16:40:00 and 18:11:40 UTC on 11 May 2011. The top and bottom of a box represents the 75th and 25th percentiles, respectively, the middle line represents the median, the bottom whisker represents the smallest data point within 1.5 times the inter-quartile range (IQR)., the top whisker is the largest data point still within 1.5 times IQR, and the small circles represents data outside 1.5 times the IQR. The fifth leg was divided according to when the temperature was below 0 °C (a) and when the temperature was at or above 0 °C (b).

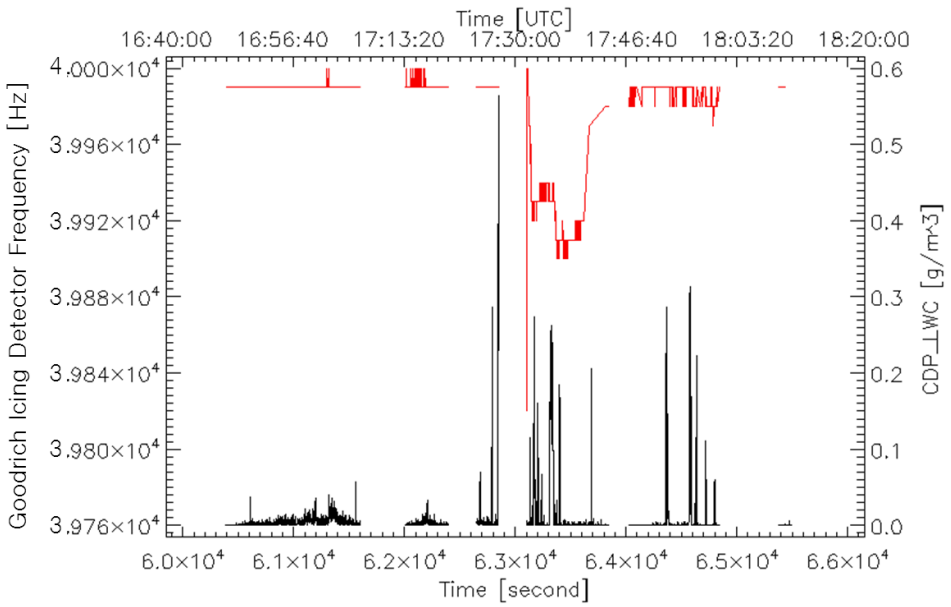

Figure 32: Cloud Droplet Probe (CDP) calculated liquid water content (LWC) in black and Goodrich Icing Detector Frequency (red) during the six level flight legs on 11 May 2011.

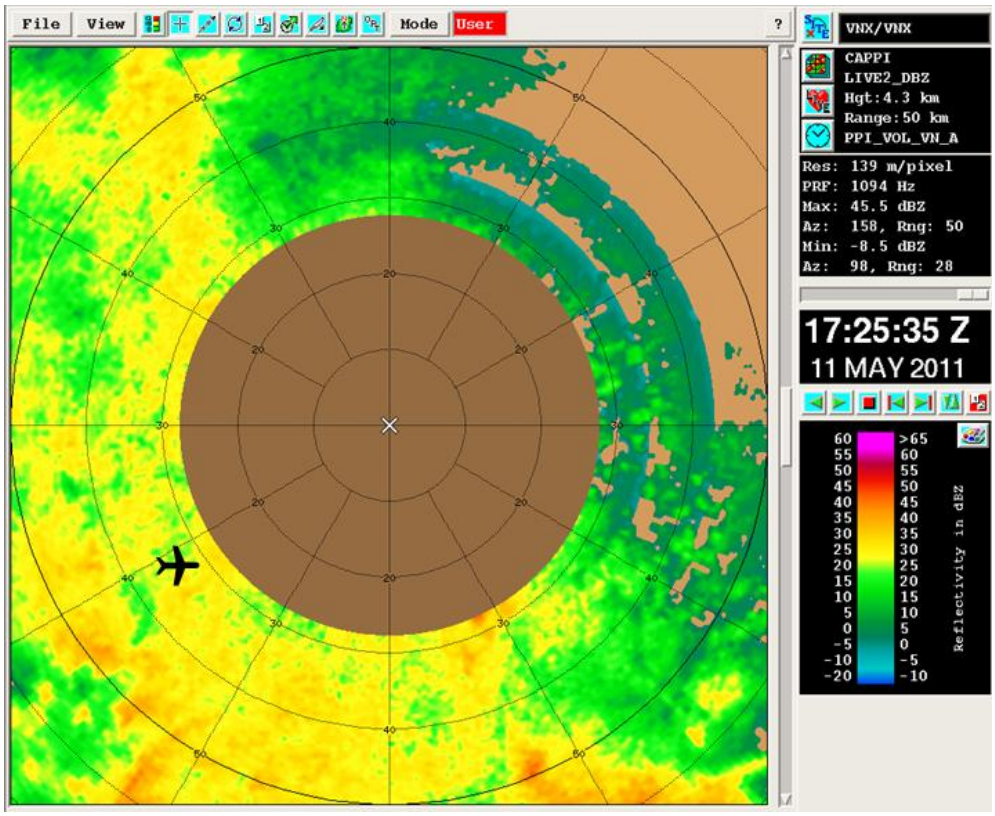

Figure 33: CAPPI showing radar reflectivity at 4.6 km MSL at 17:30 UTC. Black airplane symbol denotes the position of the UND Citation at 17:31 UTC.

Figures 34 through 40 show the variation of gamma-fit parameters to cloud particle spectra with respect to temperature, relative humidity, total water content, and λ. In the case of bimodal spectra, only the gamma fit parameters from the second (larger-sized) mode are used in this analysis. N_0 and λ decrease with increasing temperature above the melting layer (Figs. 34 and 35), which is probably due to aggregation of ice particles as they fall through the stratiform region. The decrease in N_0 and λ indicate that there are fewer total particles at lower altitudes than at higher altitudes and that there is an increasing fraction of large particles compared with the total distribution (broader spectrum). Aggregation at or above the melting layer is indicated in sample 2DC images during the first five level flight legs (Fig. 36). McFarquhar et al. (2007) showed that there was a similar trend of decreasing λ with increasing temperature in TS MCSs, concluding that the decrease in λ was caused by aggregation occurring in the stratiform regions of TS MCSs.

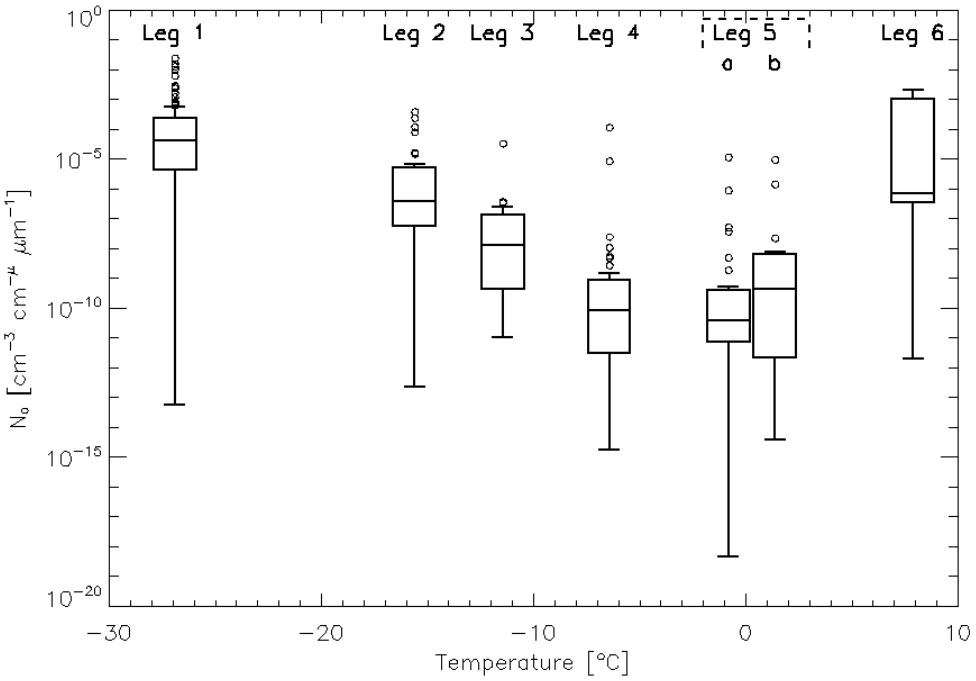

Figure 34: Boxplot showing variation of gamma intercept parameter (N_0) as a function of temperature between 16:40:00 and 18:11:40 UTC on 11 May 2011. The top and bottom of a box represents the 75th and 25th percentiles, respectively, the middle line represents the median, the bottom whisker represents the smallest data point within 1.5 times the inter-quartile range (IQR), the top whisker is the largest data point still within 1.5 times IQR, and the small circles represents data outside 1.5 times the IQR. The fifth leg is divided according to when the temperature was below 0 °C (a) and when the temperature was at or above 0 °C (b).

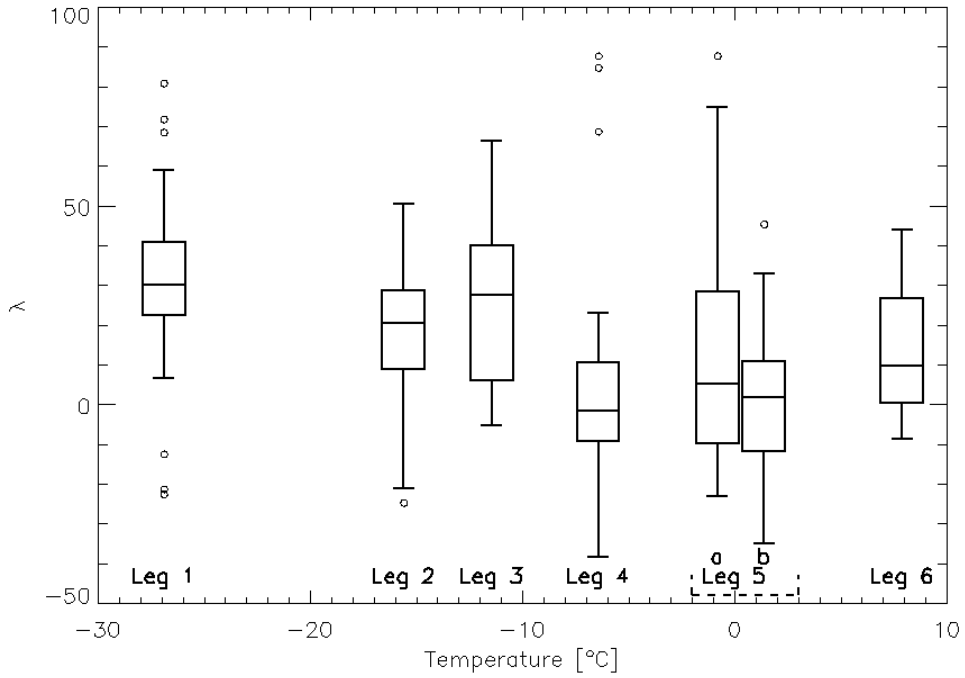

Figure 35: Boxplot showing variation of slope parameter (λ) as a function of temperature between 16:40:00 and 18:11:40 UTC on 11 May 2011. The top and bottom of a box represents the 75th and 25th percentiles, respectively, the middle line represents the median, the bottom whisker represents the smallest data point within 1.5 times the inter-quartile range (IQR), the top whisker is the largest data point still within 1.5 times IQR, and the small circles represents data outside 1.5 times the IQR. The fifth leg is divided according to when the temperature was below 0 °C (a) and when the temperature was at or above 0 °C (b).

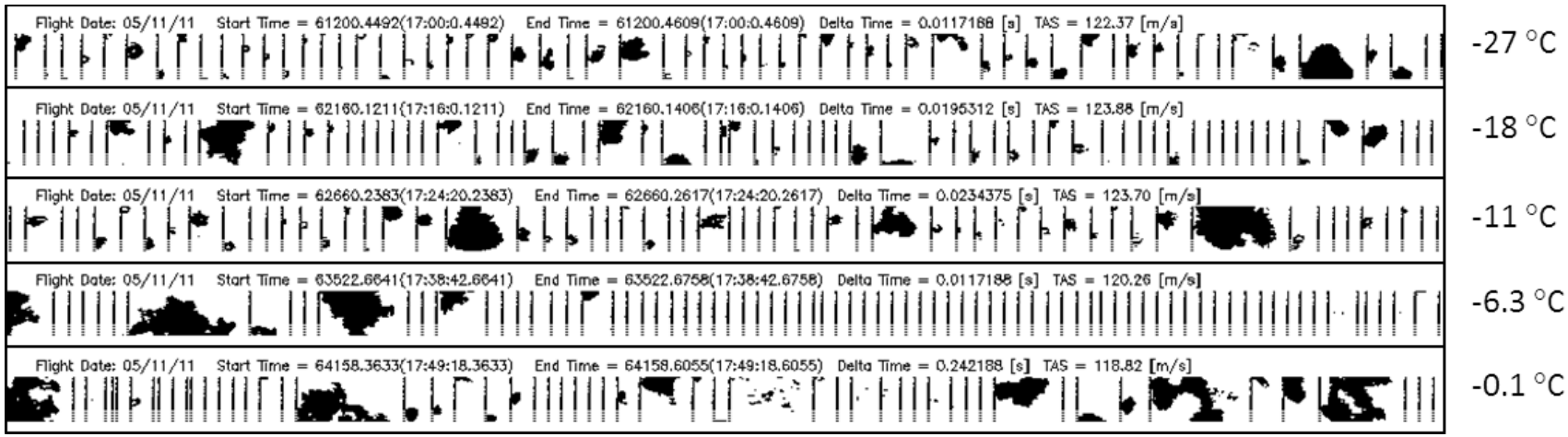

Figure 36: Examples of two-dimensional cloud (2DC) probe images and mean temperature of the corresponding leg in order (top to bottom) of descending height when the Citation was at or above the melting layer on 11 May 2011. Vertical lines are timing bars.

N_0 and λ are strongly correlated (Fig.37). For regions with uniform water content, individual distributions can vary from having many small hydrometeors (large N_0 and large λ) to having fewer, but larger-sized hydrometeors (small N_0 and small λ). Thus, the positive correlation between N_0 and λ is reasonable. Figures 38 and 39 show that both N_0 and λ increase with increasing TWC, suggesting that for a given altitude, hydrometeors will be smaller and more numerous in regions of higher TWC than in regions of lower TWC, which is consistent with the findings of McFarquhar et al. (2007).

Figure 40 shows that there is a strong positive correlation between μ and λ that was also observed by McFarquhar et al. (2007). The order of fit parameter, μ, is the parameter that adjusts the type of distribution that is present (gamma versus exponential distribution), which suggests that distributions with a larger fraction of big hydrometeors (small λ) also have a steep decrease in the smallest hydrometeors (diameters less than 100 μm). This is because when $\mu < 0$ the distribution is concave upward.

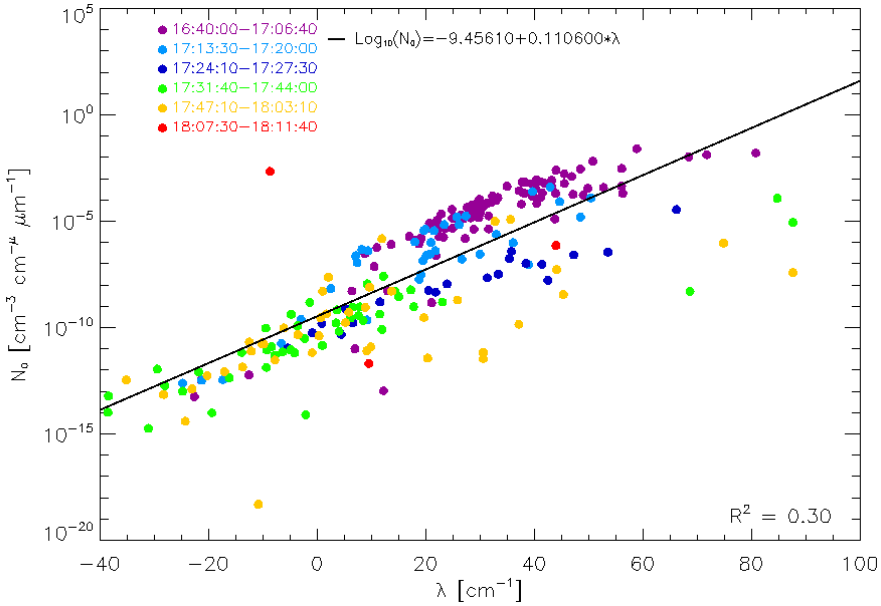

Figure 37: Variation of gamma intercept parameter (N_o) with slope parameter (λ) for 10-second fits of observed number distributions between 16:40:00 and 18:11:40 UTC on 11 May 2011. Black line represents the best fit to all of the data from the six level flight legs.

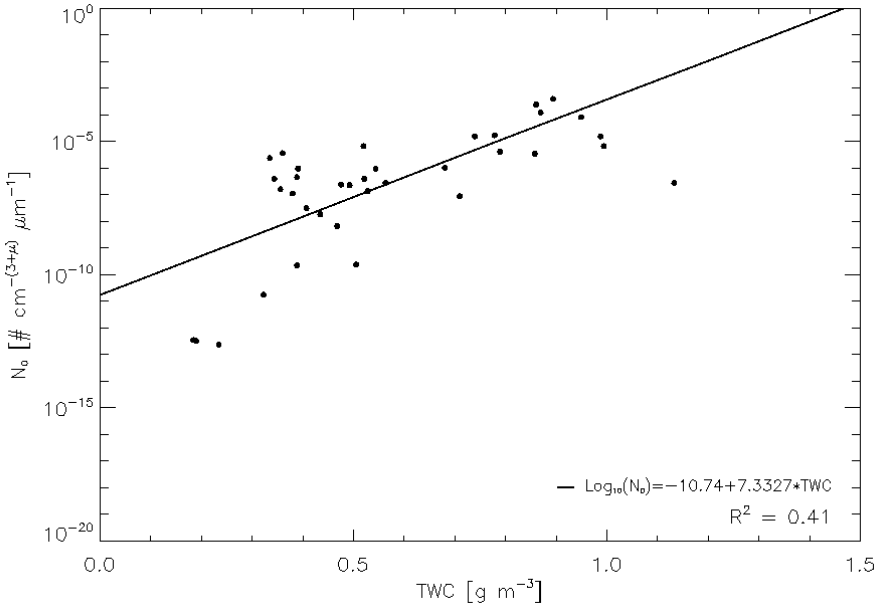

Figure 38: Variation of gamma intercept parameter (N_0) as a function of total water content (TWC) for 10-second fits of observed number distributions between 17:13:30 and 17:20:00 UTC (second flight leg) on 11 May 2011. Black line represents the best fit to all the data from the six level flight legs.

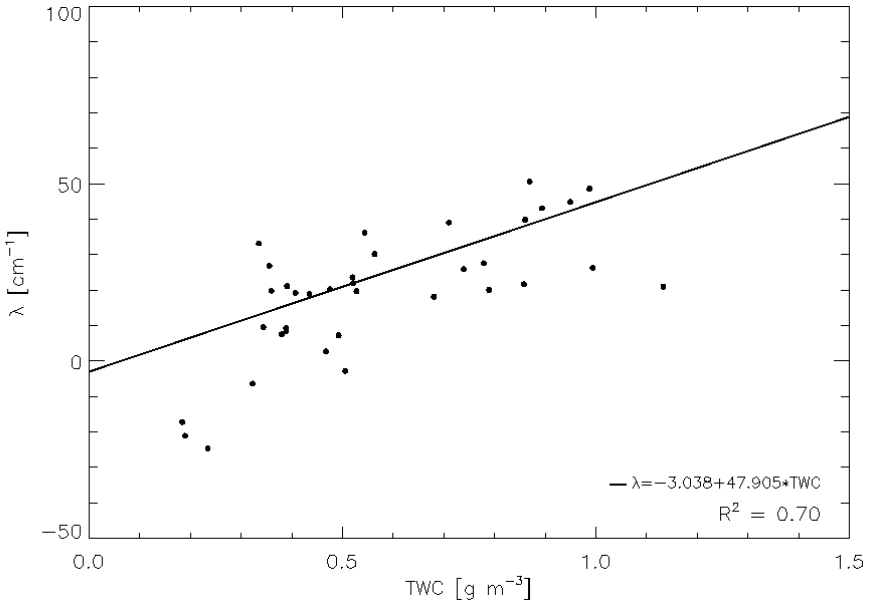

Figure 39: Variation of slope parameter (*λ*) as a function of total water content (TWC) for 10-second fits of observed number distributions between 17:13:30 and 17:20:00 UTC (second flight leg) on 11 May 2011. Black line represents the best fit to all the data from the six level flight legs.

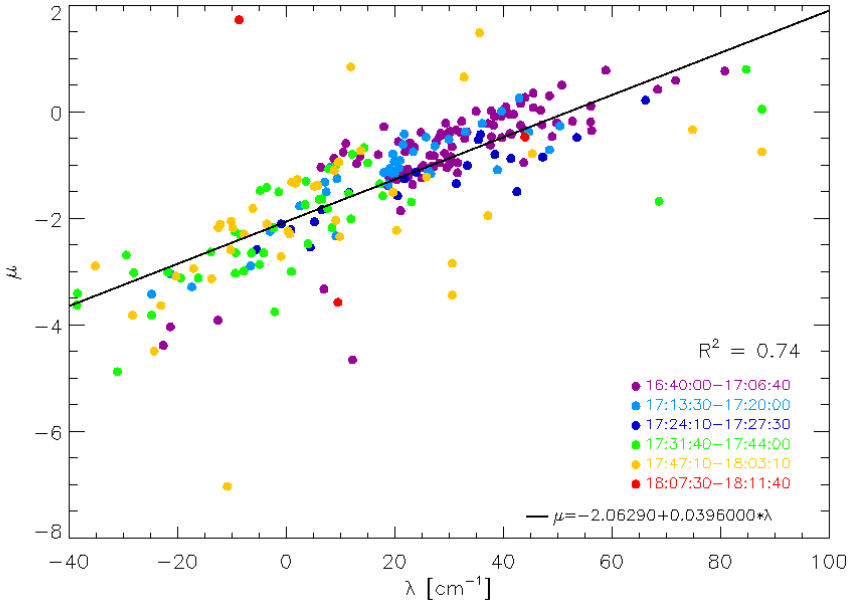

Figure 40: Variation of order of fit parameter (*μ*) as a function of slope parameter (*λ*) for 10-second fits of observed number distributions between 16:40:00 and 18:11:40 UTC on 11 May 2011. Black line represents the best fit to all the data from the six level flight legs.

McFarquhar et al. (2007) reported that λ ranged from 0 to 20 cm^{-1}, μ varied between -2 and 0, and N_0 ranged from 10^{-4} to 10^{-1} $cm^{-(3+\mu)}$ μm. The range of all three gamma parameters (N_0, μ, λ) for the 11 May MCS was larger than the range reported in McFarquhar et al. (2007). Table 6 shows that 25% of the λ values fell within the range that McFarquhar et al. (2007) reported. A little over half (54%) of the spectra in this study have larger λ (larger slopes) while about 21% of the spectra had smaller λ (smaller slopes) than what McFarquhar et al. (2007) reported. When values of λ are restricted to between -10 °C and 0 °C to better compare with the temperature range McFarquhar et al. (2007) reported, then the percentage of values within 0 and 20 cm^{-1} is about 35% (Table 7). This suggests that the portion of stratiform regions in BAMEX between -10 and 0 °C contained a higher percentage of smaller particles (compared to the total spectrum) than the same region in the parallel stratiform region in this study.

Table 6: The total number of ten-second data points during the six level flight legs, the number and percentage of points within the range of values found by McFarquhar et al. (2007), the number and percentage above these values, and the number and percentage below.

	Total Number	% within	% above	% below
N_0	244	17.2	0	82.8
μ	244	63.1	10.7	26.2
λ	244	25.4	53.7	20.9

Table 7: The total number of ten-second data points during the six level flight legs that occurred when the temperature was between -10 and 0 °C, the number and percentage of points within the range of values found by McFarquhar et al. (2007), the number and percentage above these values, and the number and percentage below.

	Total Number	% within	% above	% below
N_0	71	1.4	0	98.6
μ	71	39.4	4.2	56.3
λ	71	35.2	16.9	47.9

Almost all of the N_0 values in this study were below the range found in McFarquhar et al (2007) (Tables 6 and 7). Eighty-three percent of all N_0 values (Table 6) in this case study and 99% of N_0 values when the temperature was between -10 and 0 °C (Table 7) were below the N_0 values reported in McFarquhar et al. (2007). This suggests that there were fewer hydrometeors present in the PS MCS than in the BAMEX TS MCSs. However, the mean observed total number concentration (N_t) from the 2DC is 0.412 cm^{-3}, which is an order of magnitude greater than the mean N_t reported in McFarquhar et al. (2007) and unlike the comparison of N_0 in Tables 6 and 7; furthermore, it suggests there were more hydrometeors in the PS MCS than in the TS MCS. An explanation for the discrepancy is that nearly all of the spectra were found to be bimodal and since only the gamma fit parameters from the larger mode were used in this analysis, the contribution of the smallest (and most numerous) particles are effectively ignored and therefore N_0 may not always be representative of N_t. A comparison between the mean TWC in this study (0.39 g m^{-3}) and the mean TMC from McFarquhar et al. (2007) (1.44 g m^{-3}) shows there is less hydrometeor mass in the PS MCS than in the BAMEX trailing stratiform regions. This suggests that the hydrometeors in the PS MCS were less dense than in the BAMEX MCSs, there were fewer larger hydrometeors present in the PS MCS (supported by the lower N_0 values in this study), or both.

One possible reason for the large range of λ in this study (-40 to 90 cm^{-1}) is due to the different spectral widths. McFarquhar et al. (2007) used spectra constructed

from two instruments (a 2DC and a two-dimensional precipitation (2DP) probe), which included particles with diameters between 50 μm and 6.4 mm. The sizes of the hydrometeors used in this study are between 30 μm and 3 mm. It is expected that by using a wider spectrum, the extremes of λ will disappear.

Sixty-three percent of the μ values found in this study fall within the range found by McFarquhar et al. (2007), while only 39% of μ values – when the temperature was between -10 and 0 °C – was within their range of data. Most of the rest were lower than what was reported by McFarquhar et al. (2007). This also supports the conclusion that there were a larger fraction of larger hydrometeors compared to smaller ones in BAMEX than in this case study.

There are some differences between McFarquhar et al. (2007) and this study that should be considered to the above conclusions. 1) The first is the differences in instrumentation. McFarquhar et al. (2007) used a 2DC and a 2DP to measure the hydrometeor number distributions out to 7 mm, whereas this study used only data from a 2DC. This limits the width of the spectra, which could allow more extremes of the gamma fit parameters to be determined, as mentioned earlier. 2) The 2DC in MC3E was outfitted with Korolev tips, to which McFarquhar et al. (2007) make no reference; thus, this study assumes that the 2DC and 2DP in BAMEX were not outfitted with the Korolev tips. 3) This study uses the Nevzorov probe to measure the total water content of the MCS, whereas McFarquhar et al. (2007) use mass-dimensional relationships applied to the particle size distributions, constrained by estimates of radar reflectivity, to derive

the mass of the particles. Since TWC and TMC are derived from two different methods, differences between these two quantities do not necessarily mean that the clouds are dissimilar. 4) Differences in data processing between McFarquhar et al. (2007) and this study could lead to different conclusions as well. McFarquhar et al. (2007) used a single particle rejection criterion (particles with an area ratio less than 0.2 were rejected) whereas the 2DC data used in this study had multiple criteria for rejection. 5) Spectra in McFarquhar et al. (2007) were averaged into sixty-second intervals, effectively smoothing the spectra by a factor of six more than this study, further reducing the possibility of extreme gamma fit parameter values. 6) McFarquhar et al. (2007) did not account for bimodality in the data; they fit only a single gamma distribution to the entire spectrum width.

CHAPTER 5: SUMMARY AND CONCLUSIONS

Parker and Johnson (2000) classified MCSs into three types: trailing stratiform, leading stratiform, and parallel stratiform. Many studies have been conducted on TS MCSs, but not on LS and PS MCSs. In PS MCSs, Parker (2007) found that storm-relative hydrometeor advection towards the left of the convective line (relative to the storm motion vector) produces a line-parallel precipitation region. These MCSs also produce a cold pool in close proximity to the surface outflow boundary and evolve into TS MCSs after this occurs. On 11 May 2011, a PS MCS was sampled using multiple platforms including rawinsondes, radar, and aircraft as it traversed across the MC3E project domain, enabling a detailed case study of this event.

At 12 UTC, a longwave trough was in place over the western United States at 300 hPa with a jet stream extending from New Mexico to North Dakota. This set up a favorable convective environment over the southern plains (Texas, Oklahoma, and Kansas), with a surface low pressure system centered over the Oklahoma panhandle. A cold front and a preceding dryline were oriented north-to-south over western Texas. Several shortwaves at multiple levels of the atmosphere helped provide lift and overcome the strong "cap" in place over Oklahoma and northern Texas, sustaining convection throughout the morning hours. Through the day, upper-level divergence,

ample CAPE, and decreasing 800 hPa temperatures sustained the convection, helping to regenerate it at 16 UTC. A cold pool developed after 18 UTC, expanding southward and westward. The cold pool intensified as the MCS transitioned from a PS to TS MCS.

Conclusions from this study are:

- Southerly winds present over Oklahoma and southern Kansas above 2 km MSL were likely responsible for creating the PS characteristics in the MCS.
- Line-parallel winds and line-perpendicular wind components in the eastern half of the MCS were similar to those in a simulated PS MCS from Parker (2007). In the western half of the MCS, an area of 5-10 m s^{-1} line-perpendicular westerly inflow may have signaled the presence of a rear-inflow jet, a feature not seen in Parker (2007).
- A southeasterly inflow entrained sub-saturated pre-storm air into the front portion of the MCS, causing sub-saturated conditions during the end of the fourth and the beginning of the fifth level flight legs.
- There was very little LWC present in the stratiform region. The only LWC above the melting layer was found at the end of the third flight leg, when the Citation was flying near some embedded convection in the parallel stratiform region.
- N_0 and λ decreased with increasing temperature and N_0 decreased with decreasing λ, indicating that aggregation was occurring in the stratiform region.

- There were lower total concentrations of hydrometeors in the 11 May parallel stratiform region compared to the trailing stratiform regions in BAMEX, considering that the majority of N_0 values in this study were lower than the values reported in McFarquhar et al. (2007). In addition, a large portion of μ and λ values were lower in this study than in McFarquhar et al. (2007), showing that there is a greater fraction of larger hydrometeors in the 11 May parallel stratiform region than in the BAMEX trailing stratiform regions.
- Trends in the TWC and the gamma distribution parameters with respect to height and the correlations between the distribution parameters are similar to trends found in McFarquhar et al. (2007), indicating that microphysical processes occurring in TS MCSs are similar to those in this PS MCS.

This case study found many similarities between the observed PS MCS and the one simulated using a numerical model, suggesting that the basic elements of these MCSs are understood. Features such as the possible rear inflow jet and the embedded convection in the parallel stratiform region were not seen in the simulation and more research in these areas is needed. This case study also suggests that the basic microphysical processes of the parallel stratiform region are the same as the processes in trailing stratiform regions. More research is needed to determine if this is true for the majority of PS MCSs. Finally, additional research is also needed to determine whether

differences in microphysical properties could result in any significant kinematic differences in MCS types.

REFERENCES

Davis, C., and Coauthors, 2004: The Bow Echo and MCV Experiment: Observations and opportunities. *Bull. Amer. Meteor. Soc.*, **85**, 1075-1093.

Delene, D. cited 2012: University of North Dakota's Citation Aircraft Wind Calculation Aircraft Wind Equations. [Available at http://aerosol.atmos.und.edu/ADPAA/winds/Winds_Equation.html]

Delene, D. J., 2011: Airborne Data Processing and Analysis Software Package. *Earth Science Infomatics*, **4**, 29-44.

Gallus, W. A., N. A. Snook, and E. V. Johnson, 2008: Spring and Summer Sever Weather Reports over the Midwest as a Function of Convective Mode: A Preliminary Study. *Wea. Forecasting*, **23,** 101-113.

Garrett, T. J., A. J. Heymsfield, M. J. McGill, B. A. Ridley, D. G. Baumgardner, t. P. Bui, and C. R. Webster, 2004: Convective generation of cirrus near the tropopause. *J. Geophys. Res.*, **109**.D21203, doi:10.1029/2004JD004952.

Gayet, J.-F., J. Ovarlez, V. Shcherbakov, J. Ström, U. Schumann, A. Minikin, F. Auriol, A. Petzold, and M. Monier, 2004: Cirrus Cloud Microphysical Properties at Southern and Northern Midlatitudes during the INCA Experiment. *J. Geophys. Res.*, **109**.D20206, doi: 10.1029/2004JD004803.

Glickman, T. S. Ed., 2000: *Glossary of Meteorology.* 2nd ed. Amer. Meteor. Soc., 855 pp.

Halligan, E. A., and M. D. Parker, 2004: 22 June 2003 BAMEX Observations of a Convective Line with Parallel Precipitation. *22nd Conf. on Severe Local Storms,* Hyannis, MA, Amer. Meteor. Soc.

Heymsfield, A. J., and J. L. Parrish, 1978: A Computational Technique for Increasing the Effective Sampling Volume of the PMS Two-Dimensional Particle Size Spectrometer. *J. Appl. Meteor.*, **17,** 1566-1572.

Heymsfield, A. J., L. M. Miloshevich, C. Schmitt, A. Bansemer, C. Twohy, M. R. Poellot, A. Fridlind, and H. Berber, 2005: Homogeneous Ice Nucleation in Subtropical and

Tropical Convection and Its Influence on Cirrus Anvil Microphysics. *J. Atmos. Sci.*, **62**, 41-64.

Houze, R. A., Jr., B. F. Smull, and P. Dodge, 1990: Mesoscale Organization of Springtime Rainstorms in Oklahoma. *Mon. Wea. Rev.*, **118,** 613-654.

Houze, R. A., Jr., S. A. Rutledge, M. I. Biggerstaff, and B. F. Smull, 1989: Interpretation of Doppler Weather Radar Displays of Midlatitude Mesoscale Convecive Systems. *Bull. Amer. Meteor. Soc.*, **70,** 608-619.

Jensen, M. P. and coauthors, 2010: Midlatitude Continental Convective Clouds Experiment (MC3E). DOE Report DOE/SC-ARM/10-004, 43 pp.

Jensen, E. J. and coauthors, 2005: Ice supersaturations exceeding 100% at the cold tropical tropopause: implications for cirrus formation and dehydration. *Atmos. Chem. Phys.,* **5**, 851-862.

Korolev, A., *Probe Tips for Airborne Instruments Used to Measure Cloud Microphysical Parameters*, United States Patent No. 7 861 584, Issued: 4 January 2011, Owner: Her Majesty the Queen in Right of Canada, a Represented by the Minister of Environment.

Korolev, A. V., J. W. Strapp, G. A. Isaac, and A. N. Nevzorov, 1998: The Nevzorov airborne hotwire LWC-TWC probe: Principles of operation and performance characteristics. *J. Atmos Oceanic Technol.*, **15**, 1495-1510.

Lenschow, D. H., 1986: Aircraft measurements in the boundary layer. *Probing the Atmospheric Boundary Layer,* D. H. Lenschow, Ed., Amer. Meteor. Soc., 39-55 pp.

May, R. D., 1998: Open-path, near-infrared tunable diode laser spectrometer for atmospheric measurements of H_20. *J. Geophys. Res.*, **103.D15** 161-19,172.

McFarquhar, G. M., M. S. Timlin, R. M. Rauber, B. F. Jewett, J. A. Grim, and D. P. Jorgensen, 2007: Vertical Variability of Cloud Hydrometeors in the Stratiform Region of Mesoscale Convective Systems and Bow Echoes. *Mon. Wea. Rev,* **135,** 3405-3428.

Moller, A. R., C. A. Doswell III, M. P. Foster, and G. R. Woodall, 1994: The Operational Recognition of Supercell Thunderstorm Environments and Storm Structures. *Wea. Forecasting,* **9,** 327-347.

Mostafa, M., J. Hutton, B. Reid, 2001: GPS/IMU products – the Applanix approach. D. Fritsch and R. Spiller, Eds. *Photogrammetric Week 2001*, Wichmann Verlag, Heidelberg, Germany, 63-83.

National Oceanic and Atmospheric Administration's National Weather Service Radar Operations Center, cited 2012: WSR-88D Dual Polarization Deployment Progress as of 4/11/12. [Available at http://www.roc.noaa.gov/WSR88D/PublicDocs/DualPol/DPstatus.pdf]

NOAA, cited 2012: FSL Output Format Description. [Available at http://www.esrl.noaa.gov/raobs/intl/fsl_format-new.cgi].

Parker, M. D., 2007: Simulated Convective Lines with Parallel Stratiform Precipitation. Part I: An Archetype for Convection in Along-Line Shear. *J. Atmos. Sci.*, **64,** 267-288.

Parker, M. D., and R.H. Johnson, 2000: Organizational Modes of Midlatitude Mesoscale Convective Systems. *Mon. Wea. Rev.*, **128,** 3413-3436.

Parker, M. D., S. A. Rutledge, and R. H. Johnson, 2001: Cloud-to-Ground Lightning in Linear Mesoscale Convective Systems. *Mon. Wea. Rev.*, **129,** 1232-1242.

Parker, M. D. and R. H. Johnson, 2004a: Structures and Dynamics of Quasi-2D Mesoscale Convective Systems. *J. Atmos. Sci.*, **61,** 545-567.

Parker, M. D., and R. H. Johnson, 2004b: Structures and dynamics of quasi-2d mesoscale convective systems. *J. Atmos Sci.*, **61,** 545-567.

Petersen, W. A., and M. P. Jensen, 2012: Physical Validation of GPM Retrieval Algorithms Over Land: An Overview of the NASA-DOE Mid-Latitude Continental Convective Clouds Experiment (MC3E). *18th Conf. on Satellite Meteorology, Oceanography, and Climatology*, New Orleans, LA, Amer. Meteor. Soc.

Press, W. H., S. A. Teukolsky, W. T. Vetterling, and B. P. Flannery, 1992: *Numerical Recipes in FORTRAN: The Art of Scientific Computing.* Cambridge University Press, 963 pp.

Rotunno, R., J. B. Klemp, and M. L. Wisman, 1988: A theory for strong, long-lived squall lines. *J. Atmos Sci.*, **45,** 463-485.

Schumacher, R. S., and R. H. Johnson, 2005: Organization and Environmental Properties of Extreme-Rain-Producing Mesoscale Convective Systems. *Mon. Wea. Rev.*, **133,** 961-976.

Smith, A. M., G. M. McFarquhar, R. M. Rauber, J. A. Grim, M. S. Timlin, and B. F. Jewett, 2009: Microphysical and Thermodynamic Structure and Evolution of the Trailing Stratiform Regions of Mesoscale Convective systems during BAMEX. Part I: Observations. *Mon. Wea. Rev.*, **137,** 1165-1185.

Stickney, T. M., M. W. Shedlov, D. I. Thompson, and F. T. Yakos, 1981: Rosemount total temperature sensors. Tech. Rep. 5755, 28 pp. [Available from Rosemount Engineering Company, P. O. Box 35129, Minneapolis, MN 55435.].

Storm, B. A, M. D. Parker, and D. P. Jorgensen, 2007: A Convective Line with Leading Stratiform Precipitation from BAMEX., *Mon. Wea. Rev.*, **135,** 1769-1785.

Storm Prediction Center, cited 2012: Explanation of SPC Severe Weather Parameters. [Available at http://spc.noaa.gov/exper/mesoanalysis/help/begin.html]

Ström, J, B. Strauss, T. Anderson, F. Schröder, J. Heintzenberg, and P. Wendling, 1997: In Situ Observations of the Microphysical Properties of Young Cirrus Clouds. *J. Atmos. Sci.*, **54,** 2542-2553.

Thompson, G, cited 2012: stations.txt. [Available at http://weather.rap.ucar.edu/surface/stations.txt]